Design and Prototyping of a Pneumatically Enabled Haptic Device

By

Alireza Akhoondi Asadi

A Thesis submitted to the Faculty of Graduate Studies in

partial fulfillment of the requirements for the degree of

Master of Science

Department of Mechanical Engineering

Faculty of Engineering

University of Manitoba

Winnipeg, Manitoba, Canada

July 2017

ABSTRACT

The field of telerobotics is quickly progressing towards more intelligent and autonomous systems. Haptic devices are key tools to perform the teleoperation and are therefore an important area of research. The main objective of this thesis was to develop a new haptic device that has high force capability, low inertia, high power-to-weight ratio and small size. This haptic device uses pneumatic actuators in order to fulfill some of the mentioned characteristics. These actuators were mounted inside the structure's arms. Each arm provides one degree of freedom. First, a number of arm-actuating configurations were introduced in order to create the necessary background for the device design. Next, the final design of the haptic device was introduced and prototyped. All the materials used in final prototype are commercially available, or can be produced using a laser cutter. This makes the device eligible for rapid prototyping. Moreover, it is able to create maximum force of 1.96 lbf (8.75 N) (in orthogonal position) while the *PHANTOM Omni*, commercial available haptic device similar to the developed device in terms of weight and size, has 0.75 lbf (3.3 N) maximum force capability.

ACKNOWLEDGMENTS

First and foremost, I would like to thank my supervisor Professor Nariman Sepehri. I would also like to thank my co-advisor Dr. Sean O'Brien. Their expertise, knowledge and kindness helped me a lot throughout my Master's program. It has been a privilege for me working under their supervisions.

I would like to thank my friends, Ramhuzaini Abd Rahman, Ali Maddahi and Vikram Banthia for their support during my research.

I would like to thank Professor Witold Kinsner for giving me an excellence point of view in computer systems. I would like to thank Dr. Ehsan Jalayeri, Mr. Irwin Penner, and Mr. Daniel Rossong for their great help during the fabrication process of the prototype device.

No words can describe my heartfelt thanks to my parents, Hamid and Fatemeh, and my sisters Maryam and Negar, for the lifetime supports and encouragements.

Dedication

To my father, mother and sisters, with love

TABLE OF CONTENTS

LIST OF FIGURES

LIST OF TABLES

1. INTRODUCTION

1.1. Statement of the problem

Teleoperation refers to the operation of a system at a distance. This is one of the first and most challenging domain of robotics [1]. Nikola Tesla [2] developed one of the first teleoperation systems in the late 18 century. He developed an apparatus to control the movement of a vehicle. Manipulation at a distance was one of the first usage of teleoperation Since that time give the robot semiautonomous capabilities; however, human operator controls the task itself [2]. Therefore, the operator uses a manipulator called *Master* to control the second environment called *Slave*. Contact force information is provided to the operator in order to improve the telecommunication performance [1].

Fig. 1. Teleoperation of a robotic manipulator (source: http://www.alamy.com).

Magnetic Resonance Imaging (MRI) is a critically important imaging method for many medical applications. However, devices that operate in such an environment require some limitations to be imposed on materials and actuator choice. This is because of the strong magnetic field that exists

inside the MRI and that any existing magnetic object can easily distort the image [3]. Designing a proper haptic device as a master for use in MRI applications is important since it can play an important role in functional MRI (fMRI) in diagnostic and basic neuroscience [4].

Pneumatic actuators were chosen to be used in this thesis to develop a new haptic device. This is because of the fact that pneumatic actuators have low maintenance costs, high level of force to weight ratio, low inertia, and are commercially available in non-magnetic material. Hydraulic actuators have some disadvantages compared to pneumatic actuators in haptic device design. For example, pneumatic actuators have the highest power to weight ration for transferring masses up to 20kg [5].

1.2. Objectives and Layout

The primary objective of this thesis was to design and fabricate a haptic device that has following characteristics: (i) provide effective force-feedback, (ii) is made of low-cost materials, (iii) is easy to build, and (iv) has a reasonable small size.

The major questions to be answered in this thesis are as follows:

1. How can the designed haptic device be capable of handling required forces?
2. Can the proposed haptic device be made of non-magnetic materials and compact enough to be used in MRI applications?
3. Is the proposed prototyping process fast enough for rapid prototyping purposes?

The outline of this thesis is as follows: Chapter 1 provides an introduction and discusses the problem statement and proposed solution. Chapter 2 provides an overview of the teleoperation and haptic devices that have been developed so far. Design and prototyping of the haptic device is

discussed in Chapter 3. Chapter 4 is presents experimental results. Chapter 5 provides the conclusions.

2. LITERATURE REVIEW

Haptic devices have been used in applications including remote surgery, surgical training, teleoperation and rehabilitation. Depending on the application, there are different characteristics required for haptic device. The literature has previously described some improvements of haptic devices including: device structure [6], [7], workspace [8] and force-feedback [9],[10].

2.1. Background on Teleoperation

Teleoperation is useful when there are restrictions to access the remote environment e.g. pressure, temperature and distance [2]. Teleoperation applications have expanded during past years. In early 1990, teleoperation was used by astronauts to control a multisensory robot on board the space-craft (ROTEX) [11]. Teleoperation has also been used to implement a force-reflecting controller for a mobile hydraulic equipment [12]. Teleoperation creates safe and efficient work environment for underwater applications [13]. It is also used in telesurgery to replace or augment hand instruments [14].

A high performance teleoperation requires means to provide kinesthetic feedback to the human operator [9]. Force-feedback gives tactile information from the remote environment to the human operator [2]. The information is necessary for the operator to make decisions and take actions at the remote environment.

2.2. Background on Haptics

Haptic is the science of creating touch sensation. It is derived from the Greek word “haptesthai”. Haptesthai means sense of touch [15]. Humans use the haptic sense to touch, explore, manipulate

and perceive objects. Haptic is a distinguished sense among human being's senses because of its bilateral nature. It can receive from and do work upon an environment [16].

Haptic and robotic technologies are deeply connected due to the common foundation of mechanism design, actuating, sensing and control. Haptic interface are used to recreate or improve the tactile experiences through mechatronic devices. It involves force interaction with human. This experience can be with either a real environment or a simulated one.

Haptic technology is quickly growing and expanding as many new applications are adding to it each day. Haptic devices have been developed and used in many fields e.g. teleoperation, robotic surgery and computer-aided design [17]. Haptic devices receive inputs from Human operators. These inputs are usually position and force. These inputs are applied to the virtual or real-environment. The response of the environment then goes through the models, sensing and estimations. Eventually, the haptic device actuators apply the corresponding forces (touch sensations) to the human body. An ideal haptic device creates the real sensation for the human user. This means that it makes the human users feel like they are interacting with the environment themselves. This goal requires a very complicated mechanism and controller for a haptic device [18].

2.3. Haptic Device Structure

Haptic device structures are designed based on their application. They usually have multiple Degrees of Freedom (DOF). Haptic devices with 6-DOF may have the best performance because human hand is capable of sensing in all the possible 6-DOFs in 3D space.

Haptic device mechanisms are divided into serial and parallel structures. Serial structures are composed of a sequence of multiple links and joints called chain. Serial chains start at a point and

end at another point called the end-effector. Some of the commercially available haptic devices have used by researchers such as Phantom Omni [19], Premium and Geomagic touch X [20].

Fig. 2. Geomagic Touch, serial haptic device (source: [21]).

As shown in Fig. 2, Geomagic Touch is a 6-DOF serial haptic device. All of the joints used in this structure are revolute [22]. Its kinematic chain starts from the base, which is connected to the ground, and ends at the end-effector.

Parallel structures consist of multiple kinematic chains. These chains are connected together and support the end-effector [18], [23]. Some of the commercially haptic devices have used parallel structures to increase the stiffness and force capabilities.

Fig. 3. Omega.3 haptic device (source: [24]).

Using a commercially available haptic device might not be practical because of special characteristics that are necessary for some applications. For example, in [25] a new 6-DOF haptic device was introduced using two, three DOF parallel structures. These two parallel structures are connected together with a steering handle. This haptic device is designed to have low inertia and wide orientation angles and be capable of handling large force/torque feedbacks. This haptic mechanism has large orientation angles. This matches the slave workspace orientation angles. All 6 motors are placed at the base frame. This results in minimizing the system's inertia and helps providing bigger range for force and torque capabilities [25].

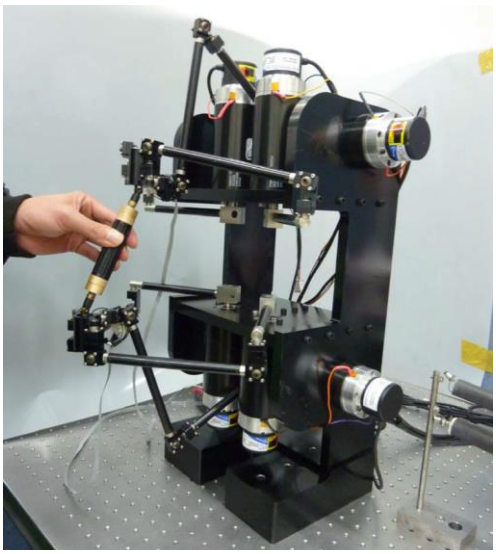

Fig. 4. Developed parallel haptic device in [25].

Proper work space, light structure and handling high forces/torques, might be the reason that researchers start developing a new haptic devices. Medical simulation is an area that researchers need to have such mentioned characteristics. Suleman *et al*. [26] compared three parallel structures in respect of their workspace and force/torque capabilities to find the optimum design solution. This structure is designed to be used in medical simulations such as bone removal by milling or drilling. However, they only considered the simulation part in addition to some analysis, and did not discuss the manufacturing and experiment challenges.

Researchers also tried to modify some parallel structures to overcome their disadvantages and reach new characteristics. Najafi and Sepehri [6], developed hand-controllers for distance ultrasound imaging. This device has 4-DOF, is kinematically decoupled and uses cable transmission to reflect the actuators force that is located on the ground.

2.4. Haptic Force-feedback

The importance of designing a high quality force-feedback system is arising significantly. This is because of the fact that safe critical applications such as surgery depend on the proper force-feedback. For instance, in remote surgery applications surgeons are separated from the patients. In this situation, the only possible tactile perception that surgeons could have from the patients is the force-feedback from the haptic device. To this end, it is necessary to develop a device with suitable force-feedback in such applications [27].

There are four ways to interface between the master and slave device in teleoperations. This includes *position-position*, *position-force*, *force-position* and *force-force* methods. The *position-force* method is used more frequently in teleoperation systems [25]. In this method, the master device controls the slave device position and orientation. Then slave device interacts with the environment. This environment can be either a real environment in which an existing robot is interacting with it [28]–[30], or a simulated computer model [31], which generates the output forces. Interaction forces would then be reflected to the master side. One of the most common ways to implement this method is to utilize the Direct Force Reflection (DFR). This approach scales and reflects the measured forces at the slave side to the master side [32]–[36]. These forces can be either monitored by sensors existing at the slave side, or an output from the simulation model.

Developing a human hand force/ torque capability model is the starting point to develop a force-feedback for a haptic device. This modeling will prevent the potential injury that a device might cause to human body. Stocco *et al*. [37] performed a study to specify the human hand force and torque capabilities. To find the best mechanism for the haptic pen, comparison between the

workspaces and force capabilities for three robot structures was proposed. All the two mechanisms have an equal workspace area; however, the Stewart platform has a large void space within its workspace because of the prismatic actuators contraction/extension limit. Eventually, the twin haptic-pantograph is used because it had the best results [37].

M. Q. Le *et al.* [38] developed 1-DOF pneumatically actuated teleoperation system. They described a new bilateral control scheme for pneumatic actuators using a simple on/off solenoid valve. Bo Yang *et al.*[3] designed and controlled an MRI compatible 1-DOF needle-driver robot. They used pneumatic actuators along with long transmission lines. Pneumatic actuators have been used in this research because of their high Signal to Noise Ratio (SNR), back-drivability and ease to maintenance. They observed that the strong magnetic field did not affect the performance of the pneumatic actuator and that the teleoperation system did not negatively affect the MRI image quality.

2.5. Summary

This chapter provided an overview of developed haptic devices for different purposes. However, the developed haptic devices so far have not provided a solution for a haptic device with small size, fast fabrication process, high force capabilities, pneumatically actuated and feasible to be built in non-magnetic material.

3. DESIGN OF DEVICE

Actuating an arm with a prismatic actuator is challenging. This is because of the actuator limitations and structure complexities. To start the design process, first, some arm-actuator configurations have been selected and analysed kinematically.

3.1. Arm Actuator Assembly

The arm design process began with a general design concept. The general design concept has multiple parameters that needed to be calculated and optimized for each arm design. This made the design process rather complicated at the beginning. The general design concept is shown in Fig. 5.

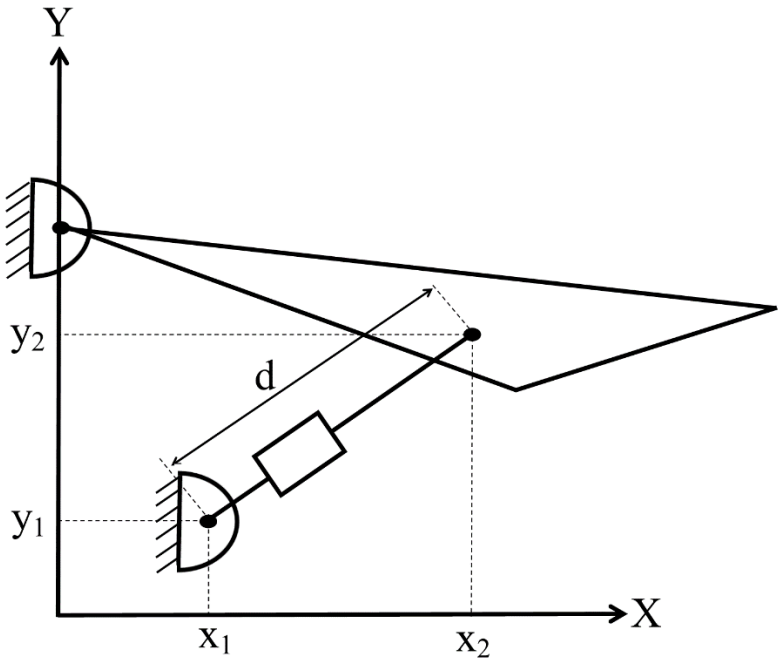

Fig. 5. Arm design concept.

As shwon in Fig. 5, the general arm actuator assembly connection has 4 parameters to define the actuator geometry. A few arm-actuator configurations were chosen to start the design process. Design requirements are established and compared for all of the arm-actuator configurations. Eventually, the device is made out of the combinations of multiple proposed arm-actuator configurations. The followings are the device design requirements:

- The arm workspace should be able to have symmetrical movement with respect to the horizontal line.
- The actuator force should be able to compensate the required force.

There is a limitation for the first feature which is the mechanical actuator's extension and contraction limits that should match the required generated angles for the symmetrical workspace.

3.1.1. Configuration One

Configuration one is shown in Fig. 6.

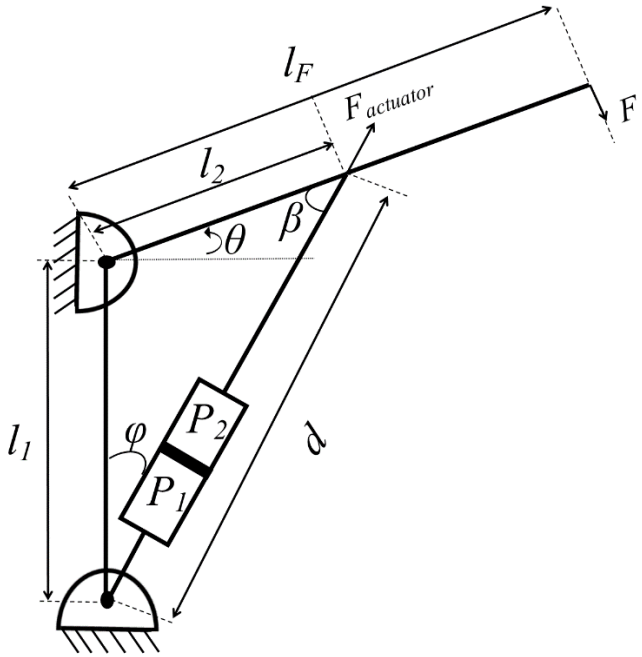

Fig. 6. Arm-actuator configuration one.

The configuration has two links (l_1 and l_2) and one actuator (d).

As described before, there is a requirement for the arm to create a symmetric motion for the second link (l_2). To this end, link lengths should be calculated to satisfy the mentioned requirement. In order to calculate the workspace region, boundary conditions are written as follows:

$$d^2 = l_1^2 + l_2^2 - 2l_1 l_2 \cos\left(\frac{\pi}{2} + \theta\right) \tag{3.1}$$

$$d_{min}^2 = l_1^2 + l_2^2 - 2l_1 l_2 \cos\left(\frac{\pi}{2} + \theta_{min}\right) \tag{3.2}$$

$$d_{max}^2 = l_1^2 + l_2^2 - 2l_1 l_2 \cos\left(\frac{\pi}{2} + \theta_{max}\right) \tag{3.3}$$

To have a symmetrical workspace for the first joint, following equation should be satisfied:

$$\theta_{max} = -\theta_{min} \tag{3.4}$$

Equations (3.2) and (3.3) can be rewritten as follows:

$$d_{min}^2 = l_1^2 + l_2^2 - 2l_1 l_2 \sin(\theta_{max}) \tag{3.5}$$

$$d_{max}^2 = l_1^2 + l_2^2 + 2l_1 l_2 \sin(\theta_{max}) \tag{3.6}$$

To calculate the lengths l_1 and l_2, Eq.(3.5) and Eq.(3.6) are added and subtracted as follows:

$$\frac{d_{min}^2 + d_{max}^2}{2} = l_1^2 + l_2^2 \tag{3.7}$$

$$\frac{d_{max}^2 - d_{min}^2}{4} = l_1 l_2 \sin(\theta_{max}) \tag{3.8}$$

Eventually, l_1 and l_2 are calculated as follows:

$$l_1 = \frac{\sqrt{\frac{d_{min}^2 + d_{max}^2}{2} + \frac{d_{max}^2 - d_{min}^2}{2\sin(\theta_{max})}} + \sqrt{\frac{d_{min}^2 + d_{max}^2}{2} - \frac{d_{max}^2 - d_{min}^2}{2\sin(\theta_{max})}}}{2} \tag{3.9}$$

$$l_2 = \frac{\sqrt{\frac{d_{min}^2 + d_{max}^2}{2} + \frac{d_{max}^2 - d_{min}^2}{2\sin(\theta_{max})}} - \sqrt{\frac{d_{min}^2 + d_{max}^2}{2} - \frac{d_{max}^2 - d_{min}^2}{2\sin(\theta_{max})}}}{2} \tag{3.10}$$

Compensating the required torque is the second design requirement. There is a maximum force limitation for any pneumatic actuator. This is due to the maximum allowable air pressure at the rear or rod side. Therefore, a proper actuator with a suitable stroke size should be chosen.

Fig. 6 shows the free-body diagram for static equilibrium considering the required force and the actuator force.

The following equation should be satisfied in order to compensate the required force.

$$F l_F \cos(\theta) = F_{actuator} l_2 \sin(\beta) \tag{3.11}$$

where β is calculated as follows:

$$\beta = \frac{\pi}{2} - (\theta + \varphi) \tag{3.12}$$

Equation (3.11) is rewritten as follows:

$$F_{actuator} = \frac{F l_F \cos(\theta)}{l_2 \cos(\theta+\varphi)} \tag{3.13}$$

Actuating force is created by the pressure at rear or ride side of the pneumatic actuator. This relationship is as follows:

$$F_{actuator} = P_1 A_1 - P_2 A_2 \tag{3.14}$$

Following equations are written to calculate the φ angle.

$$l_2^2 = d^2 + l_1^2 - 2 l_1 d \cos(\varphi) \tag{3.15}$$

$$\varphi = \cos^{-1}\left(\frac{(l_1^2+d^2)-l_2^2}{2 d l_1}\right) \tag{3.16}$$

There are different possible scenarios due to the variety of possible materials and actuators. The first chosen actuator for the arm-actuator configuration is M16D100.0U [39]. This actuator has 100 (mm) stroke and the maximum force output is 139 (N) at the rear size. Fig. 7 and Fig. 8 show the relations between the $F_{actuator}$, θ and d.

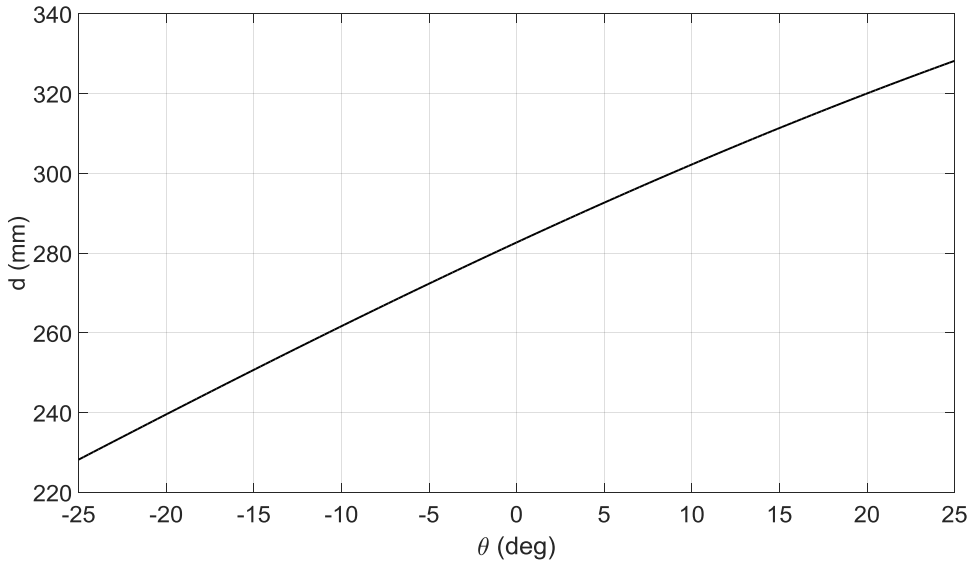

Fig. 7. Actuator stroke length at each θ for the arm-actuator configuration one, $F = 25(N), l_F = 360\ mm,\ l_F = 250\ mm, l_2 = 130\ mm\ and\ \theta_{max} = 25\ deg.$

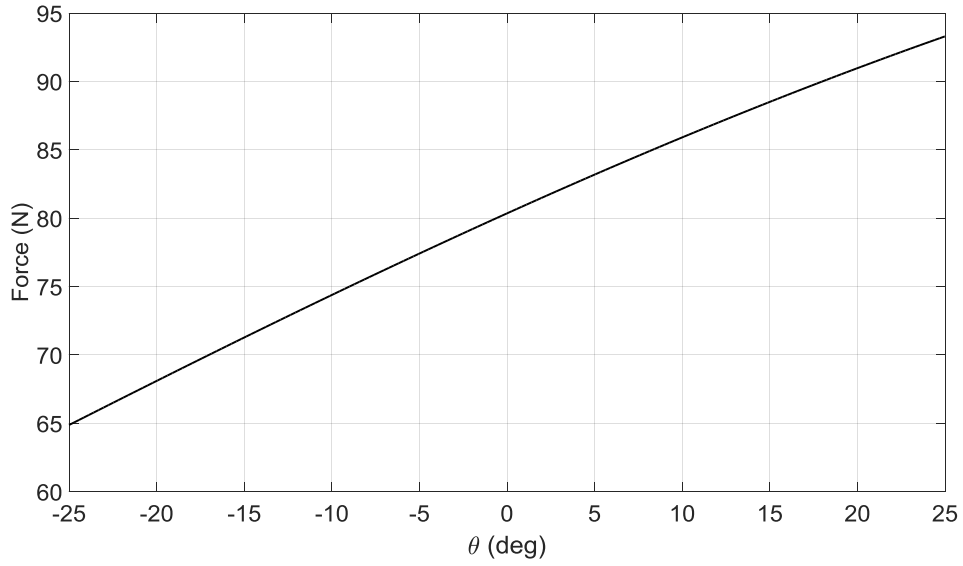

Fig. 8. Required actuating force to compensate the required force at each θ for the arm-actuator configuration one.

As shown in Fig. 8, actuator force does not exceed the maximum force limit of the chose actuator. This means that the actuator is able to compensate for the required force. However, the maximum

force is close to the limit at $\theta_{max} = 25\ (deg)$ which can be modified at the next design versions. Fig. 7 almost shows a linear behaviour between the required angle and the actuator stroke.

3.1.2. Configuration Two

The first arm-actuator configuration was able to compensate the required force within the defined angle variations. However, there are additional force requirements that add up to the required forces (e.g. gravity). This creates more limitations for the actuator to compensate the required force. To this end, the following structure is proposed in order to improve the design requirements.

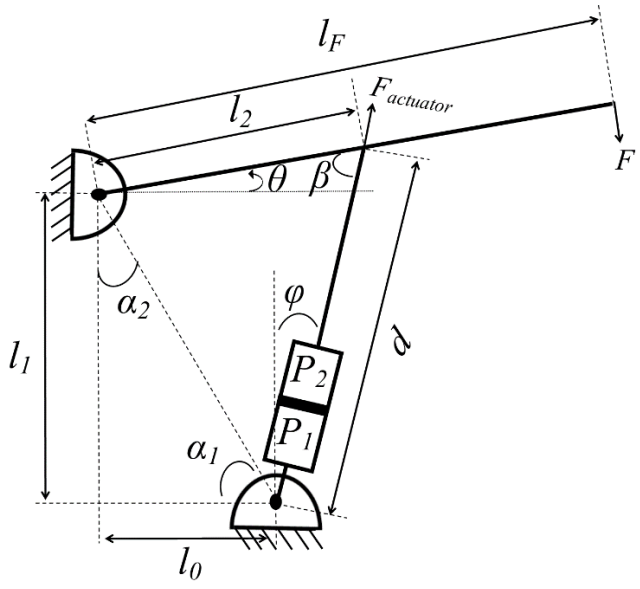

Fig. 9. Arm-actuator configuration two.

As shown in Fig. 9, the second arm-actuator configuration has four parameters that define the geometry, including l_0, l_1, l_2 and d, which is the actuator length.

In order to calculate the workspace region, boundary conditions are written as follows:

$$d^2 = l^2 + l_2^2 - 2ll_2 \cos\left(\frac{\pi}{2} + \theta - \alpha_2\right) \tag{3.17}$$

$$d_{min}^2 = l^2 + l_2^2 - 2ll_2 \cos\left(\frac{\pi}{2} + \theta_{min} - \alpha_2\right) \tag{3.18}$$

$$d_{max}^2 = l^2 + l_2^2 - 2ll_2 \cos\left(\frac{\pi}{2} + \theta_{max} - \alpha_2\right) \tag{3.19}$$

where $l = \sqrt{l_0^2 + l_1^2}$.

To have a symmetrical workspace for the second arm structure, following equation should be satisfied:

$$\theta_{max} = -\theta_{min} \tag{3.20}$$

Equations (3.18) and (3.19) can be rewritten as follows:

$$d_{min}^2 = l^2 + l_2^2 - 2ll_2 \sin(\theta_{max} + \alpha_2) \tag{3.21}$$

$$d_{max}^2 = l^2 + l_2^2 + 2ll_2 \sin(\theta_{max} - \alpha_2) \tag{3.22}$$

Following flowchart describes the procedure to calculate the arm-actuator configuration two lengths.

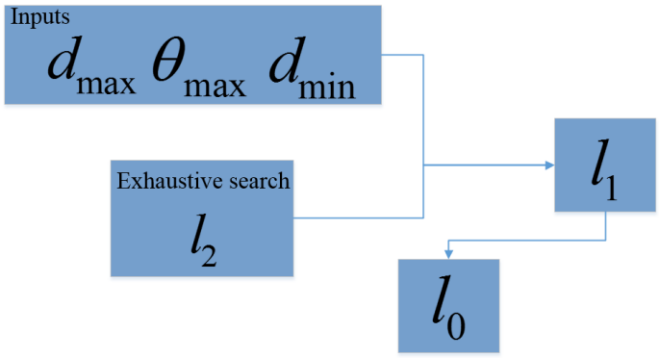

Fig. 10. Length calculation flowchart of the arm-actuator configuration two.

length l_1 is calculated as follows, by subtracting the Eq.(3.21) from Eq.(3.22):

$$l_1 = \frac{d_{max}^2 - d_{min}^2}{4l_2 \sin(\theta_{max})} \tag{3.23}$$

To calculate length l_0, Equations (3.21) and (3.22) are added up as follows:

$$\frac{d_{min}^2 + d_{max}^2}{2} = l^2 + l_2^2 + l_2(-2l_0 \cos(\theta_{max})) \tag{3.24}$$

Eventually, length l_0 is calculated as follows:

$$l_0 = \frac{2l_2 \cos(\theta_{max}) - \sqrt{4l_2^2 cos^2(\theta_{max}) + 4(\frac{d_{min}^2 + d_{max}^2}{2} - l_2^2 - l_1^2)}}{2} \tag{3.25}$$

With reference to Fig. 9, the following equation should be satisfied in order to compensate the required force.

$$F l_F \cos(\theta) = F_{actuator} l_2 \sin(\beta) \tag{3.26}$$

where β is calculated as follows:

$$\beta = (\alpha_1 + \alpha_2) - (\theta + \varphi) = \frac{\pi}{2} - (\theta + \varphi) \tag{3.27}$$

Equation (3.26) is rewritten as follows:

$$F_{actuator} = \frac{F l_F \cos(\theta)}{l_2 \cos(\theta + \varphi)} \tag{3.28}$$

Following equations are written to calculate the φ angle.

$$l_2^2 = d^2 + l^2 - 2dl \cos\left(\frac{\pi}{2} + \varphi - \alpha_1\right) \tag{3.29}$$

$$\varphi = \sin^{-1}\left(\frac{l_2^2 - (l_0^2 + l_1^2 + d^2)}{2dl}\right) + \sin^{-1}\left(\frac{l_1}{l}\right) \tag{3.30}$$

Fig. 11 and Fig. 12 show the relations between the $F_{actuator}$, θ and d for the second arm-actuator configuration.

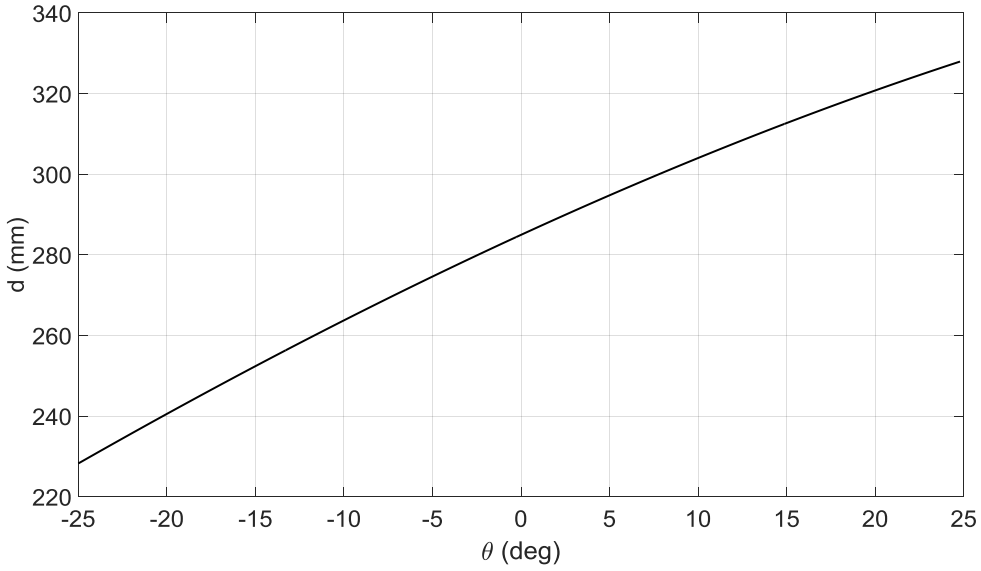

Fig. 11. Actuator stroke length at each θ for arm-actuator configuration two, $F = 25(N)$.

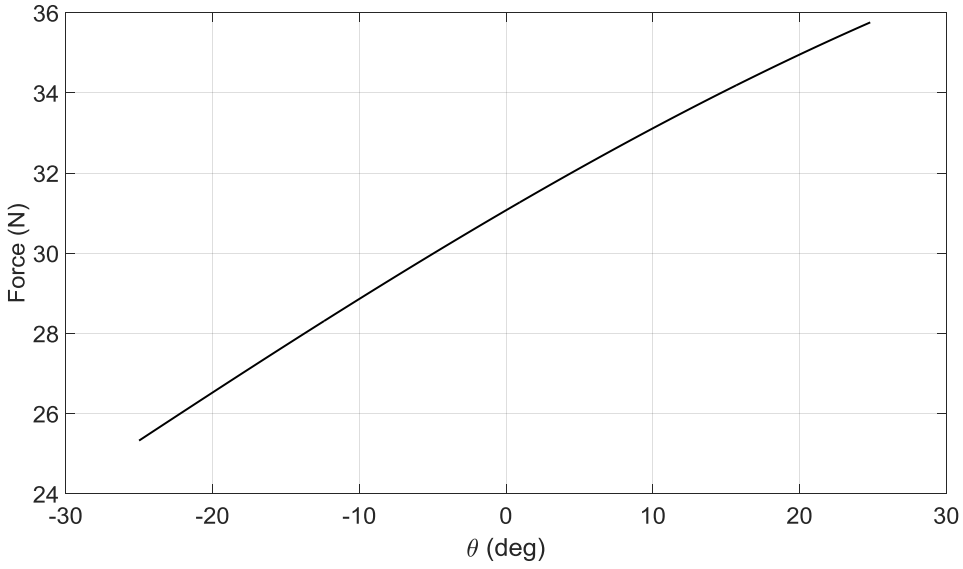

Fig. 12. Required actuating force to compensate the required force at each θ for arm-actuator configuration two.

As seen in Fig. 12, actuator force does not exceed the maximum limit for the chosen parameters. Moreover, the range of forces are lower than the first arm-actuator configuration, which is shown

in Fig. 8. This means that the actuator within the second arm-actuator configuration is able to compensate the required force better in comparison the first arm-actuator configuration. Fig. 11 shows a linear behaviour between the required angle and the actuator stroke at the second arm.

While combining the arm-actuator configurations to come up with the best manipulator device design, more arm-actuator configurations might be needed. For example, some limitations might occur regarding the actuator mounting place inside the device or movement within the structure. To this end, the second arm-actuator configuration can be modified as shown in Fig. 13.

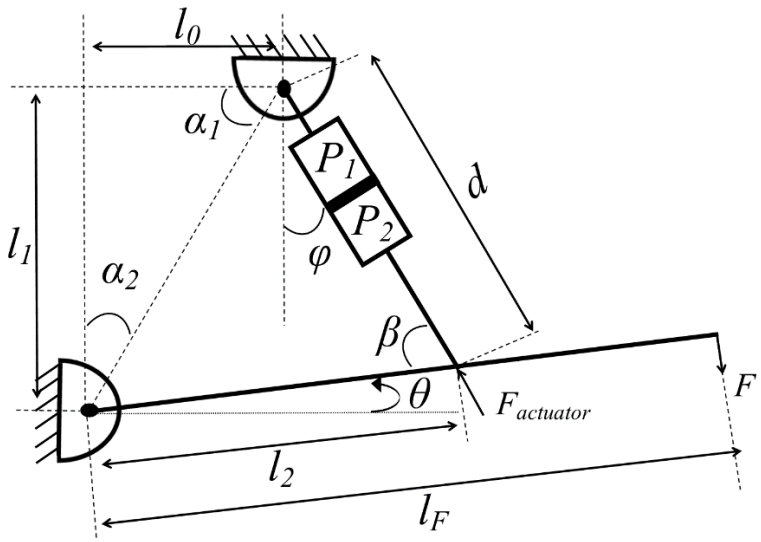

Fig. 13. Modified arm-actuator configuration two.

As shown in Fig. 13, there are four parameters that define the modified arm-actuator configuration two. This includes l_0, l_1, l_2 and d.

In order to calculate the workspace region, boundary conditions are written as follows:

$$d^2 = l^2 + l_2^2 - 2ll_2 \cos\left(\frac{\pi}{2} - \theta - \alpha_2\right) \tag{3.31}$$

$$d_{min}^2 = l^2 + l_2^2 - 2ll_2 \cos\left(\frac{\pi}{2} - \theta_{max} - \alpha_2\right) \tag{3.32}$$

$$d_{max}^2 = l^2 + l_2^2 - 2ll_2 \cos\left(\frac{\pi}{2} - \theta_{min} - \alpha_2\right) \tag{3.33}$$

where $l = \sqrt{l_0^2 + l_1^2}$.

Following equation should be satisfied to have a symmetrical workspace for the arm structure.

$$\theta_{max} = -\theta_{min} \tag{3.34}$$

Equations (3.32) and (3.33) can be rewritten as follows:

$$d_{min}^2 = l^2 + l_2^2 - 2ll_2 \sin(\theta_{max} + \alpha_2) \tag{3.35}$$

$$d_{max}^2 = l^2 + l_2^2 + 2ll_2 \sin(\theta_{max} - \alpha_2) \tag{3.36}$$

An exhaustive search was done for length l_2 in order to calculate the l_o and l_1. Length l_1 is calculated as follows, by negating the Eq.(3.35) from Eq.(3.36):

$$l_1 = \frac{d_{max}^2 - d_{min}^2}{4l_2 \sin(\theta_{max})} \tag{3.37}$$

To calculate the length l_0, Eq.(3.33) and Eq.(3.34) are added up as follows:

$$\frac{d_{min}^2 + d_{max}^2}{2} = l^2 + l_2^2 + l_2(-2l_0 \cos(\theta_{max})) \tag{3.38}$$

Eventually, l_0 is calculated as follows:

$$l_0 = \frac{2l_2 \cos(\theta_{max}) - \sqrt{4l_2^2 cos^2(\theta_{max}) + 4(\frac{d_{min}^2 + d_{max}^2}{2} - l_2^2 - l_1^2)}}{2} \tag{3.39}$$

As discussed earlier, there are limitations because of the actuator dynamics to compensate the required force. As illustrated in Fig. 13, the following equation should be satisfied in order to compensate the required force.

$$F l_F \cos(\theta) = F_{actuator} l_2 \sin(\beta) \tag{3.40}$$

where β is calculated as follows:

$$\beta = (\alpha_1 + \alpha_2) + (\theta - \varphi) = \frac{\pi}{2} + (\theta - \varphi) \tag{3.41}$$

In order to calculate the actuator force, Eq. (3.40) is rewritten as follows:

$$F_{actuator} = \frac{F l_F \cos(\theta)}{l_2 \cos(\theta - \varphi)} \tag{3.42}$$

Following equations are written to calculate the φ angle.

$$l_2^2 = d^2 + l^2 - 2dl \cos\left(\frac{\pi}{2} + \varphi - \alpha_1\right) \tag{3.43}$$

$$\varphi = \sin^{-1}\left(\frac{l_2^2 - (l_0^2 + l_1^2 + d^2)}{2dl}\right) + \sin^{-1}\left(\frac{l_1}{l}\right) \tag{3.44}$$

Following Figures describe the relations between the $F_{actuator}, \theta$ and d for the third arm configuration.

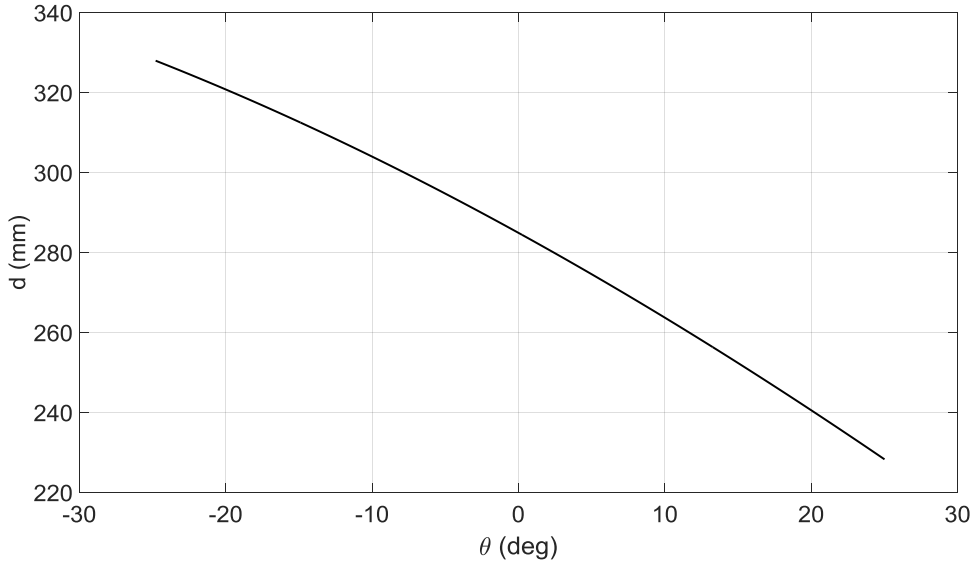

Fig. 14. Actuator stroke length at each θ for the arm-actuator configuration three, $F = 25\ N$.

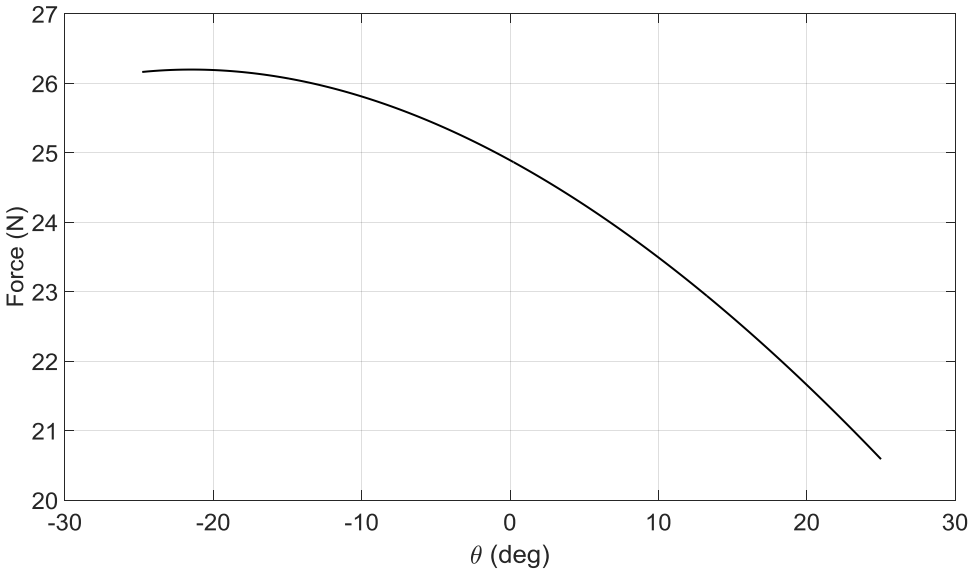

Fig. 15. Required actuating force to compensate the required force at each θ for the arm-actuator configuration three.

As illustrated in Fig. 15, actuator force limits are similar to the second arm structure, as shown in Fig. 12, and it does not exceed the maximum limit of the chose actuator. Fig. 14 shows a linear behaviour between the required angle and the actuator stroke at the third arm.

3.1.3. Configuration Three

All of the mentioned arm-actuator configurations meet the minimum design requirements which were set earlier. However, there are also other requirements that potentially emerge after the prototyping process. These include the size of haptic device. To minimize the size, there should be more parameters to optimize within the arm-actuator configuration. In order to do so, the following arm-actuator configuration is proposed.

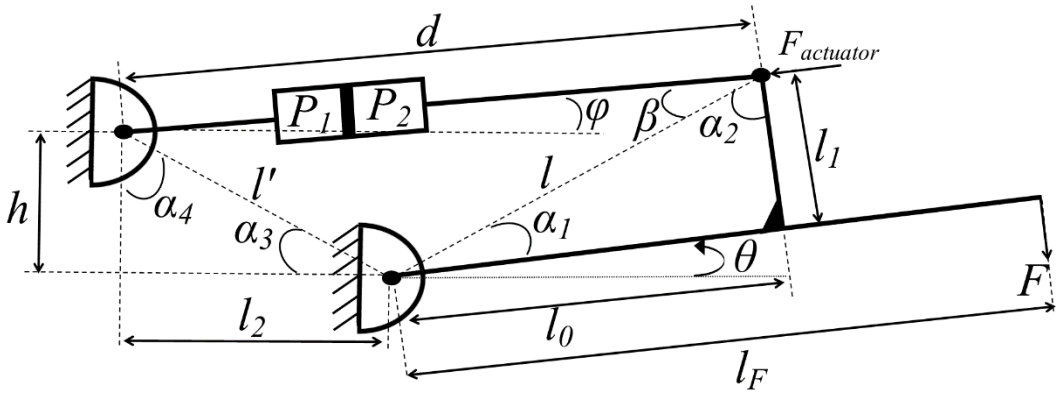

Fig. 16. Arm-actuator configuration three.

As shown in Fig. 16, there are five parameters that define the arm-actuator configuration four. This includes l_0, l_1, l_2, h and d.

In order to calculate the workspace region, boundary conditions are written as follows:

$$d^2 = l^2 + l'^2 - 2ll' \cos\left(\pi - (\theta + \alpha_1 + \alpha_3)\right) \tag{3.45}$$

$$d_{max}^2 = l^2 + l'^2 - 2ll' \cos\left(\pi - (\theta_{min} + \alpha_1 + \alpha_3)\right) \tag{3.46}$$

$$d_{min}^2 = l^2 + l'^2 - 2ll' \cos\left(\pi - (\theta_{max} + \alpha_1 + \alpha_3)\right) \tag{3.47}$$

where $l = \sqrt{l_0^2 + l_1^2}$ and $l^{'} = \sqrt{h^2 + l_2^2}$.

Equations (3.46) and (3.47) are simplified as follows:

$$d_{max}^2 = l^2 + l^{'2} + 2\cos\theta_{nax}(l_0 l_2 - h l_1) + 2\sin\theta_{nax}(l_1 l_2 + h l_0) \tag{3.48}$$

$$d_{min}^2 = l^2 + l^{'2} + 2\cos\theta_{nax}(l_0 l_2 - h l_1) - 2\sin\theta_{nax}(l_1 l_2 + h l_0) \tag{3.49}$$

Exhaustive search was done for two lengths h and l_2 to calculate the l_0 and l_1. Furthermore, there are minimum required length for h and l_2 because of the limitations that occur after manufacturing. This includes the required space to avoid the interaction between the links. Following flowchart summarizes the calculations of the third arm-actuator's lengths.

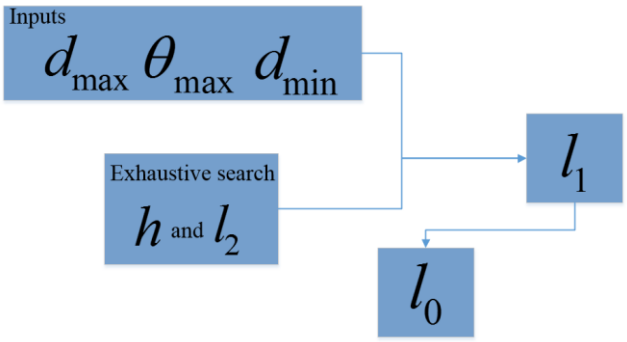

Fig. 17. Length calculation flowchart of the arm-actuator configuration three.

After some simplifications and calculations lengths l_0 is calculated as follows:

$$l_0 = \frac{-b + \sqrt{b^2 - 4ac}}{2a} \tag{3.50}$$

where a, b and c are constant values, based on design assumptions, as follows:

$$a = l^{'2} \tag{3.51}$$

$$b = 2l_2^3 \cos\theta_{nax} + 2h^2 l_2 \cos\theta_{nax} - 2h\frac{d_{max}^2 - d_{min}^2}{4\sin(\theta_{max})} \tag{3.52}$$

$$c = -2l_2 h\ cos\ \theta_{nax} \frac{d_{max}^2 - d_{min}^2}{4\ sin(\theta_{max})} + \left(\frac{d_{max}^2 - d_{min}^2}{4\ sin(\theta_{max})}\right)^2 + l^{'2} l_2^2 - 2l_2^2\ cos\ \theta_{nax} \frac{d_{max}^2 + d_{min}^2}{4\ cos(\theta_{max})} \quad (3.53)$$

Equations (3.48) and (3.49) are used again to calculate the length l_1 as follows:

$$l_1 = \frac{d_{max}^2 - d_{min}^2}{4l_2 \sin(\theta_{max})} - \frac{hl_0}{l_2} \quad (3.54)$$

As discussed earlier, required force compensation calculation is necessary because of the limitation in actuator dynamics. Following figure shows the free-body diagram under static condition. This shows the minimum required actuator force to compensate the required force.

As illustrated in Fig. 16, the following equation should be satisfied in order to hold the static equilibrium condition and compensate the required force.

$$Fl_F \cos(\theta) = F_{actuator} l_1 \sin(\alpha_2 + \beta) \quad (3.55)$$

where β is calculated as follows:

$$\beta = (\alpha_1 + \theta - \varphi) \quad (3.56)$$

In order to calculate the actuator force, Eq. (3.55) is written as follows:

$$F_{actuator} = \frac{Fl_F \cos(\theta)}{l_1 \sin(\alpha_1 + \alpha_2 + \theta - \varphi)} \quad (3.57)$$

Following equations are written to calculate the φ angle.

$$l^2 = d^2 + l^{'2} - 2dl' \cos(\varphi + \alpha_3) \quad (3.58)$$

$$\varphi = \cos^{-1}\left(\frac{h^2 + l_2^2 + d^2 - l_0^2 - l_1^2}{2dl'}\right) - \cos^{-1}\left(\frac{l_2}{l'}\right) \quad (3.59)$$

Following Figures describe the relations between the $F_{actuator}, \theta$ and d for the fourth arm configuration.

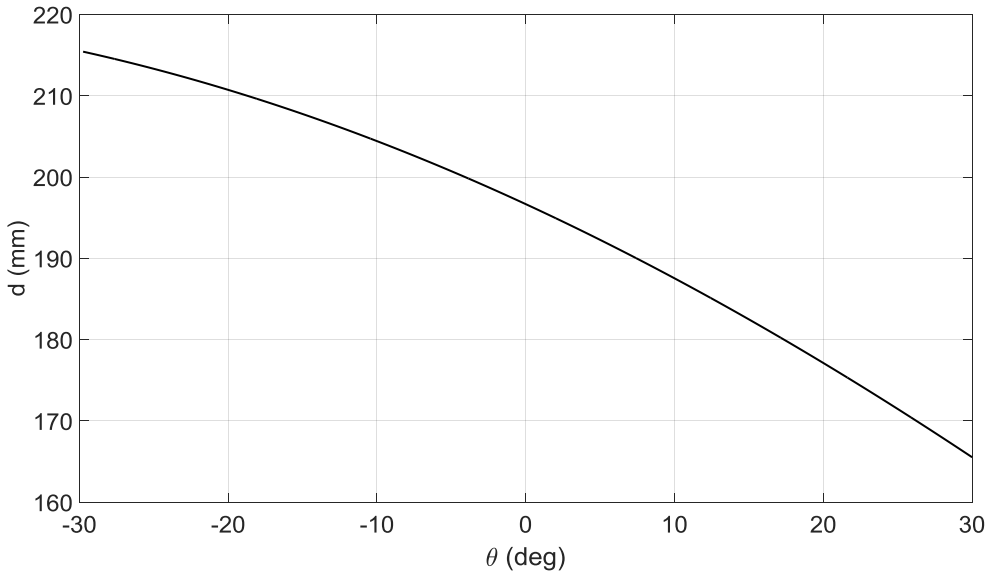

Fig. 18. Actuator stroke length at each θ for the arm-actuator configuration four, $F = 25\ N$.

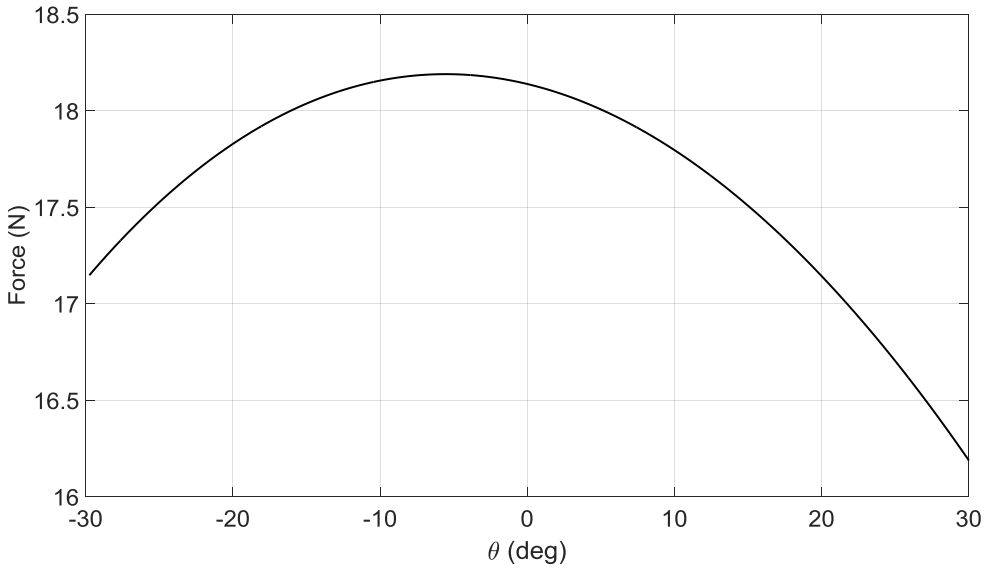

Fig. 19. Required actuating force to compensate the required force at each θ for the arm-actuator configuration four.

As illustrated in Fig. 19, actuator force supremum to compensate the required force is even lower than the second and third arm configurations as shown in Fig. 15 and Fig. 12. Fig. 18 also shows a somewhat linear behaviour between the required angle and the actuator stroke at the fourth arm. However, previous structures have shown greater extent of linear behaviour.

3.2. Manipulator Device Design

3.2.1. First Prototype

Previous arm-actuator configurations developed the foundation for the multi-arm haptic device. The first manipulator design in Fig. 20 provided 6-DOF for its end-effector.

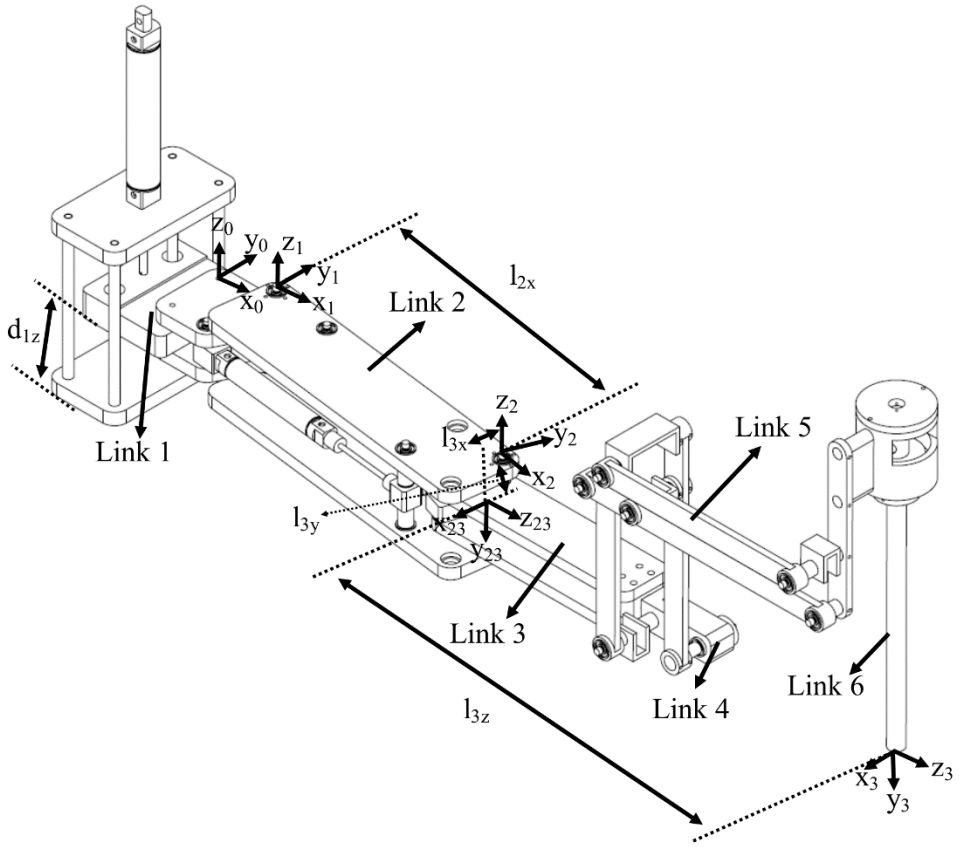

(a)

(b)

Fig. 20. First manipulator device: (a) first device design; (b) first prototype device.

The prototype of this design was built in order to see the performance of the designed mechanisms. The prototype was built using Aluminum and every attempt was made to make it light. As shown in Fig. 20, the first joint was prismatic and it defined the Z position of the end-effector. This characteristic is very important since it made the positioning controller easier to design and implement. Additionally, depth is very important for many applications. This fact becomes clearer during the kinematic analysis in next section. The second and the third joints were revolute. They rotate around the Z axis and were parallel to each other. They change the position of the end-effector in XY plane. The next three revolute joints were designed to generate the required orientation for the end-effector. A parallel structure was used in which the end-effector remains in a certain position with respect to the third joint. This main idea for this structure was first proposed in [7]. This means that the end-effector's positions and orientations are decoupled.

As shown in Fig. 20, the first, second and third coordinates are attached to the corresponding links. Note that the end-effector stays in a certain position with respect to the third joint. So, it can be assumed to be a part of the third link. Eventually, the third coordinate is attached to the end-effector.

In order to calculate the end-effector position, the transformation from the end-effector frame to the global frame is required as follows [18]:

$$^{0}r_{end-effector} = {}^{0}T_{3}\,{}^{3}r_{end-effector} \tag{3.60}$$

where $^{3}r_{end-effector}$ describes the end-effector position with respect to the third frame and $^{0}r_{end-effector}$ describes the position of the end-effector with respect to the global frame. Denavit-Hartenberg convention is used to derive the transformation matrix. Denavit-Hartenberg Table is calculated as follows:

Table 1: Denavit-Hartenberg parameter of first prototype.

#	$\boldsymbol{\theta_i}$	$\boldsymbol{d_i}$	$\boldsymbol{a_i}$	$\boldsymbol{\alpha_i}$
$0-1$	0	d_{1z}	l_{1x}	0
$1-2$	θ_1	0	l_{2x}	0
$2-23$	$\theta_2-\frac{\pi}{2}$	l_{3y}	l_{3x}	$-\frac{\pi}{2}$
$23-3$	0	l_{3z}	0	0

Based on the Denavit-Hartenberg convection, the homogenous transformation matrix between each frame is defined as follows [18]:

$$ {}^{n}T_{n+1} = \begin{bmatrix} C\theta_{n+1} & -S\theta_{n+1}C\alpha_{n+1} & S\theta_{n+1}S\alpha_{n+1} & a_{n+1}C\theta_{n+1} \\ S\theta_{n+1} & -C\theta_{n+1}C\alpha_{n+1} & -C\theta_{n+1}S\alpha_{n+1} & a_{n+1}S\theta_{n+1} \\ 0 & S\alpha_{n+1} & C\alpha_{n+1} & d_{n+1} \\ 0 & 0 & 0 & 1 \end{bmatrix} \tag{3.61} $$

where $S\theta_{n+1}$ and $C\theta_{n+1}$are the abbreviations for the sine and the cosine functions respectively.

To obtain the transformation matrix from the global frame to the end-effector frame, a successive set of homogenous transformation matrices is used as follows:

$$ {}^{0}T_{3} = {}^{0}T_{1}\,{}^{1}T_{2}\,{}^{2}T_{23}\,{}^{23}T_{3} \tag{3.62} $$

where homogenous transformation matrices are calculated, using Table 1, as follows:

$$ {}^{0}T_{1} = \begin{bmatrix} 1 & 0 & 0 & l_{1x} \\ 0 & 1 & 0 & 0 \\ 0 & 0 & 1 & d_{1z} \\ 0 & 0 & 0 & 1 \end{bmatrix} \tag{3.63} $$

$$ {}^{1}T_{2} = \begin{bmatrix} C\theta_1 & -S\theta_1 & 0 & l_{2x}C\theta_1 \\ S\theta_1 & C\theta_1 & 0 & l_{2x}S\theta_1 \\ 0 & 0 & 1 & 0 \\ 0 & 0 & 0 & 1 \end{bmatrix} \tag{3.64} $$

$$ {}^{2}T_{23} = \begin{bmatrix} S\theta_2 & 0 & C\theta_2 & l_{3x}S\theta_2 \\ -C\theta_2 & 0 & S\theta_2 & -l_{3x}C\theta_2 \\ 0 & -1 & 0 & l_{3y} \\ 0 & 0 & 0 & 1 \end{bmatrix} \tag{3.65} $$

$$ {}^{23}T_{3} = \begin{bmatrix} 1 & 0 & 0 & 0 \\ 0 & 1 & 0 & 0 \\ 0 & 0 & 1 & l_{3z} \\ 0 & 0 & 0 & 1 \end{bmatrix} \tag{3.66} $$

By using the sequence of the calculated homogenous transformation matrices, the required transformation matrix from the end-effector coordinate to the global coordinate is calculated as follows:

$$ {}^{0}T_{3} = \begin{bmatrix} C\theta_1S\theta_2 + S\theta_1C\theta_2 & 0 & C\theta_1C\theta_2 - S\theta_1S\theta_2 & X \\ S\theta_1S\theta_2 - C\theta_1C\theta_2 & 0 & S\theta_1C\theta_2 + C\theta_1S\theta_2 & Y \\ 0 & -1 & 0 & Z \\ 0 & 0 & 0 & 1 \end{bmatrix} \tag{3.67} $$

where X, Y and Z are the positions of end-effector with respect to the global frame. These positions are calculated as follows:

$$ X = l_{3z}C\theta_1C\theta_2 + l_{3x}C\theta_1S\theta_2 - l_{3z}S\theta_1S\theta_2 + l_{3x}S\theta_1C\theta_2 + l_{2x}C\theta_1 + l_{1x} \tag{3.68} $$

$$ Y = l_{3z}S\theta_1C\theta_2 + l_{3x}S\theta_1S\theta_2 + l_{3z}C\theta_1S\theta_2 - l_{3x}C\theta_1C\theta_2 + l_{2x}S\theta_1 \tag{3.69} $$

$$ Z = l_{3y} + d_{1z} \tag{3.70} $$

The workspace for the first prototype is shown in following figures. As shown in Fig. 21, the maximum cube size that could fit inside the work space has 100 mm length.

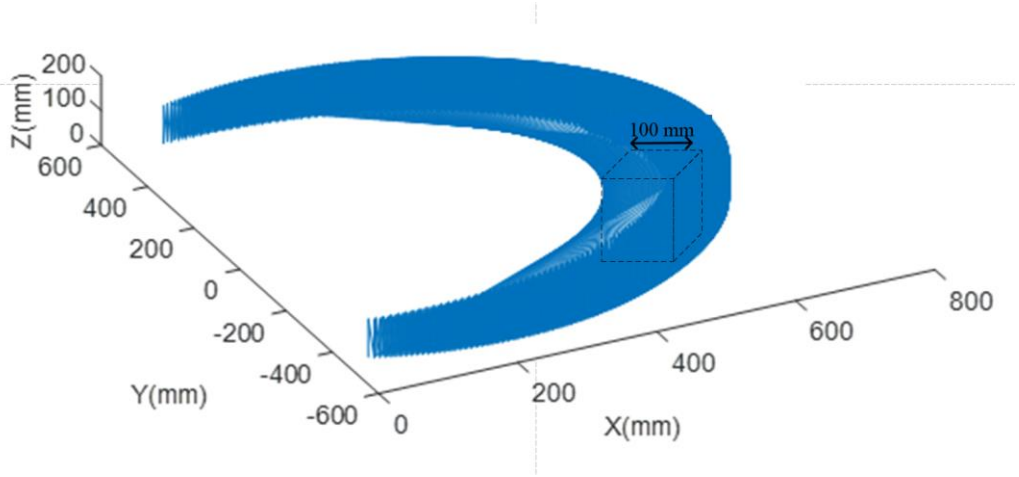

Fig. 21. 3D workspace of the first prototype. $l_{1x} = 95\ mm$, $l_{2x} = 225.01\ mm$, $l_{3x} = 12.51\ mm$, $l_{3y} = 32.86\ mm$, $l_{3z} = 351.943\ mm$, $-60° \leq \theta_1 \leq 60°$ and $-60° \leq \theta_2 \leq 60°$.

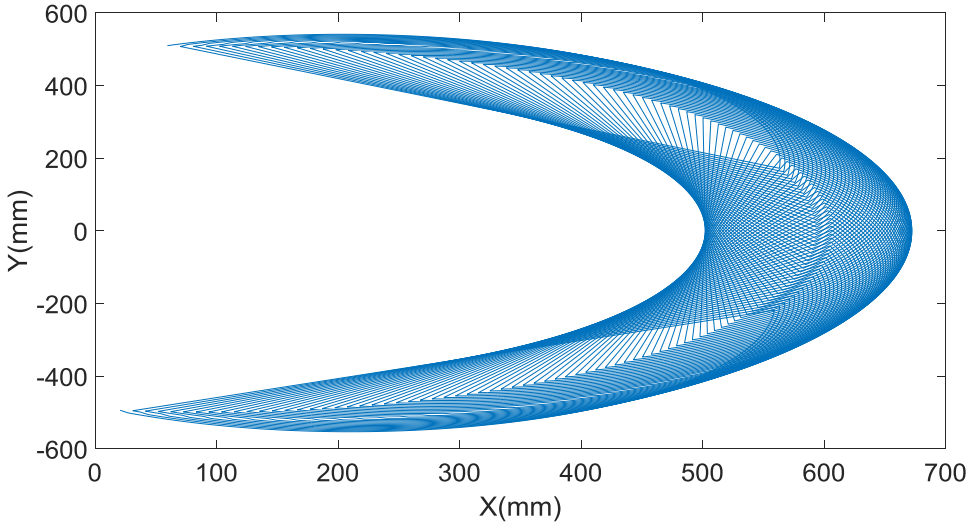

Fig. 22. Workspace of the first prototype, XY plane.

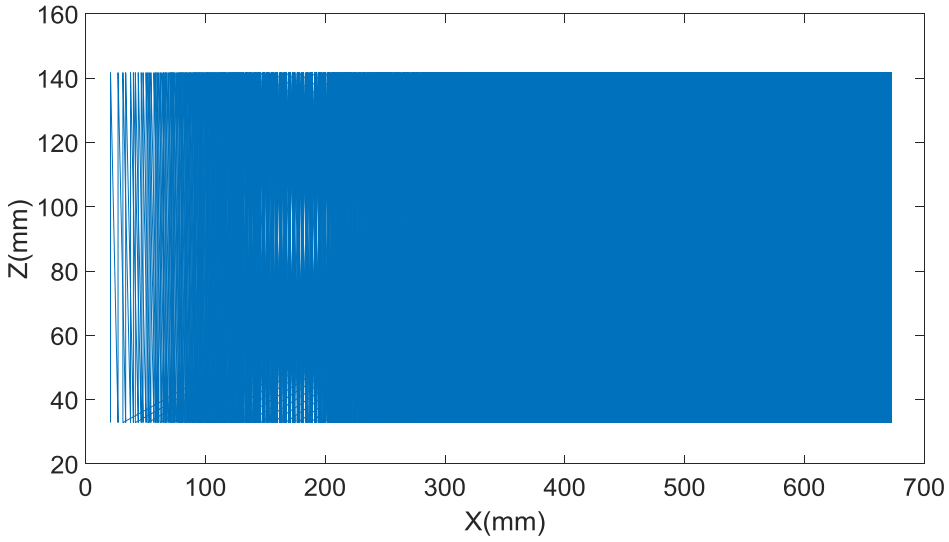

Fig. 23. Workspace of the first prototype, XZ plane.

In order to derive the end-effector velocities Jacobian matrix is used. Jacobian matrix relates the joint velocities to the end-effector velocities. This is defined as follows:

$$\begin{bmatrix} V_x \\ V_y \\ V_z \end{bmatrix} = J \begin{bmatrix} \dot{\theta}_1 \\ \dot{\theta}_2 \\ \dot{d}_{1z} \end{bmatrix} \tag{3.83}$$

To calculate the Jacobian matrix, the velocities of the end-effector are calculated as follows:

$$V_x = -\dot{\theta}_1 l_{3z} S\theta_1 C\theta_2 - \dot{\theta}_2 l_{3z} C\theta_1 S\theta_2 - \dot{\theta}_1 l_{3x} S\theta_1 S\theta_2 + \dot{\theta}_2 l_{3x} C\theta_1 C\theta_2 - \dot{\theta}_1 l_{3z} C\theta_1 S\theta_2 - \dot{\theta}_2 l_{3z} S\theta_1 C\theta_2 + \dot{\theta}_1 l_{3x} C\theta_1 C\theta_2 - \dot{\theta}_2 l_{3x} S\theta_1 S\theta_2 - \dot{\theta}_1 l_{2x} S\theta_1$$

$$V_y = \dot{\theta}_1 l_{3z} C\theta_1 C\theta_2 - \dot{\theta}_2 l_{3z} S\theta_1 S\theta_2 + \dot{\theta}_1 l_{3x} C\theta_1 S\theta_2 + \dot{\theta}_2 l_{3x} S\theta_1 C\theta_2 - \dot{\theta}_1 l_{3z} S\theta_1 S\theta_2 + \dot{\theta}_2 l_{3z} C\theta_1 C\theta_2 + \dot{\theta}_1 l_{3x} S\theta_1 C\theta_2 + \dot{\theta}_2 l_{3x} C\theta_1 S\theta_2 + \dot{\theta}_1 l_{2x} C\theta_1$$

$$V_z = \dot{d}_{1z} \tag{3.84}$$

Eventually, the Jacobian matrix is calculated as follows:

$$J = \begin{bmatrix} -l_{3z}S\theta_1C\theta_2 - l_{3x}S\theta_1S\theta_2 - l_{3z}C\theta_1S\theta_2 + l_{3x}C\theta_1C\theta_2 - l_{2x}S\theta_1 & -l_{3z}C\theta_1S\theta_2 + l_{3x}C\theta_1C\theta_2 - l_{3z}S\theta_1C\theta_2 - l_{3x}S\theta_1S\theta_2 & 0 \\ l_{3z}C\theta_1C\theta_2 + l_{3x}C\theta_1S\theta_2 - l_{3z}S\theta_1S\theta_2 + l_{3x}S\theta_1C\theta_2 + l_{2x}C\theta_1 & -l_{3z}S\theta_1S\theta_2 + l_{3x}S\theta_1C\theta_2 + l_{3z}C\theta_1C\theta_2 + l_{3x}C\theta_1S\theta_2 & 0 \\ 0 & 0 & 1 \end{bmatrix}$$

(3.85)

3.2.2. Second Prototype

The first prototype did not work well based on the users' inputs. For instance, the first prototype failed to move without substantial friction along the Z axis. Fig. 24 to Fig. 27 show the variation of the second prototype with respect to the first prototype Fig. 27.

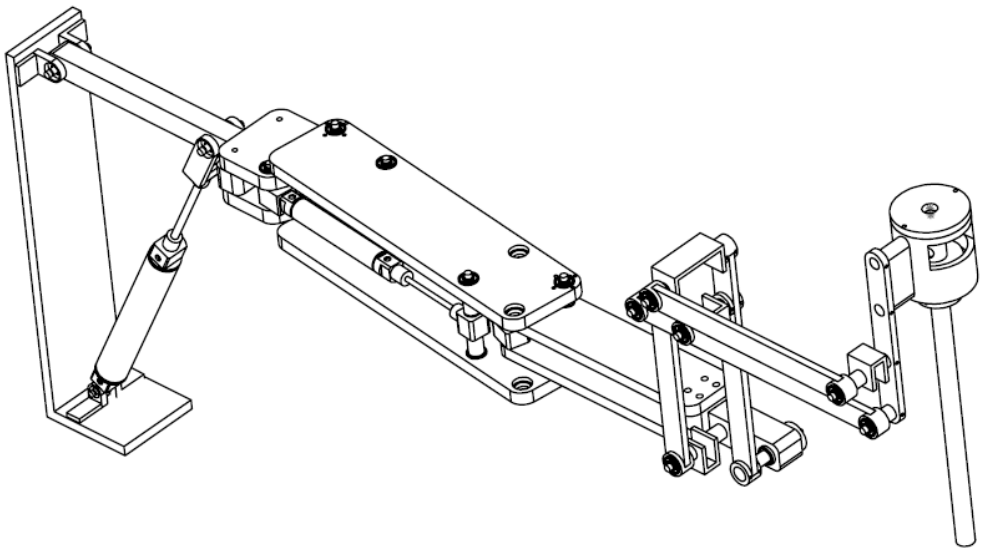

Fig. 24. Second manipulator device.

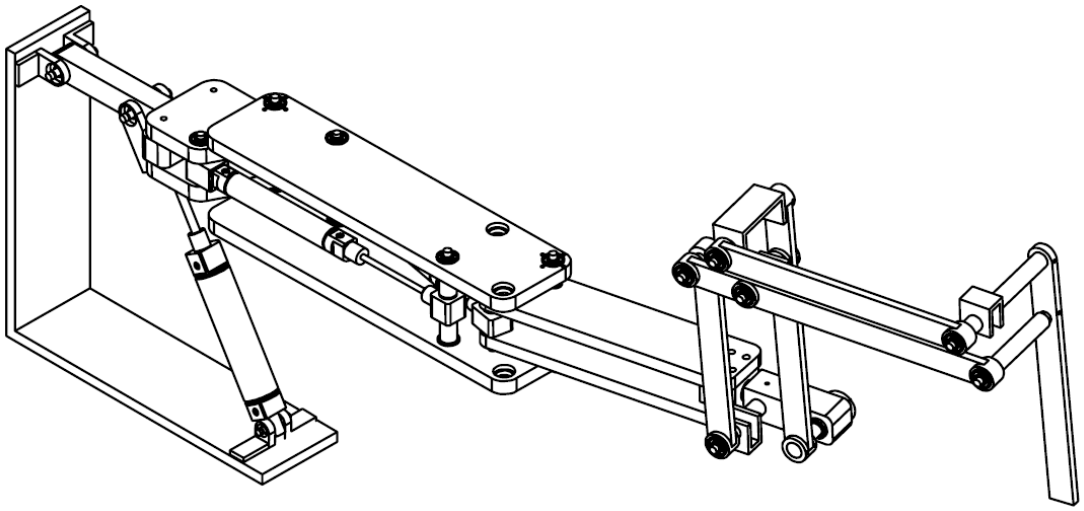

Fig. 25. Third manipulator device.

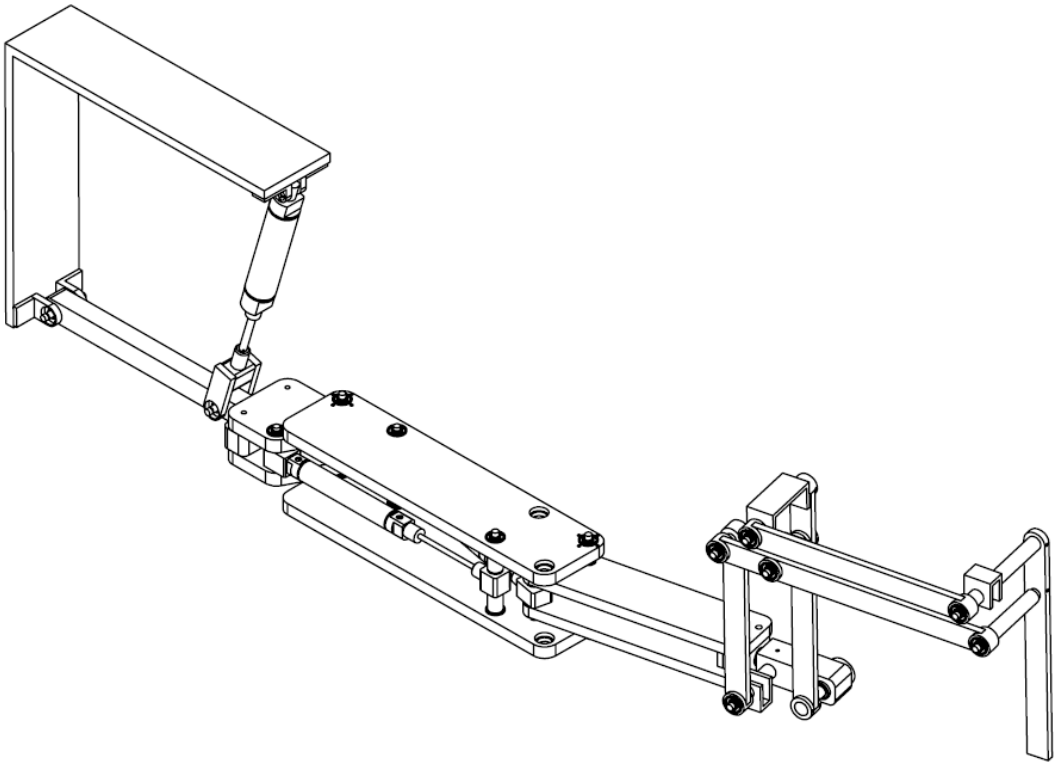

Fig. 26. Fourth manipulator device.

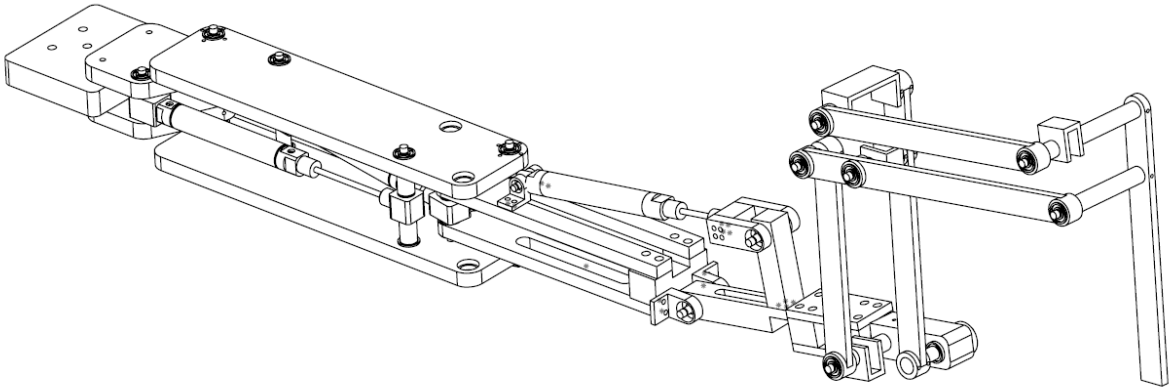

(a)

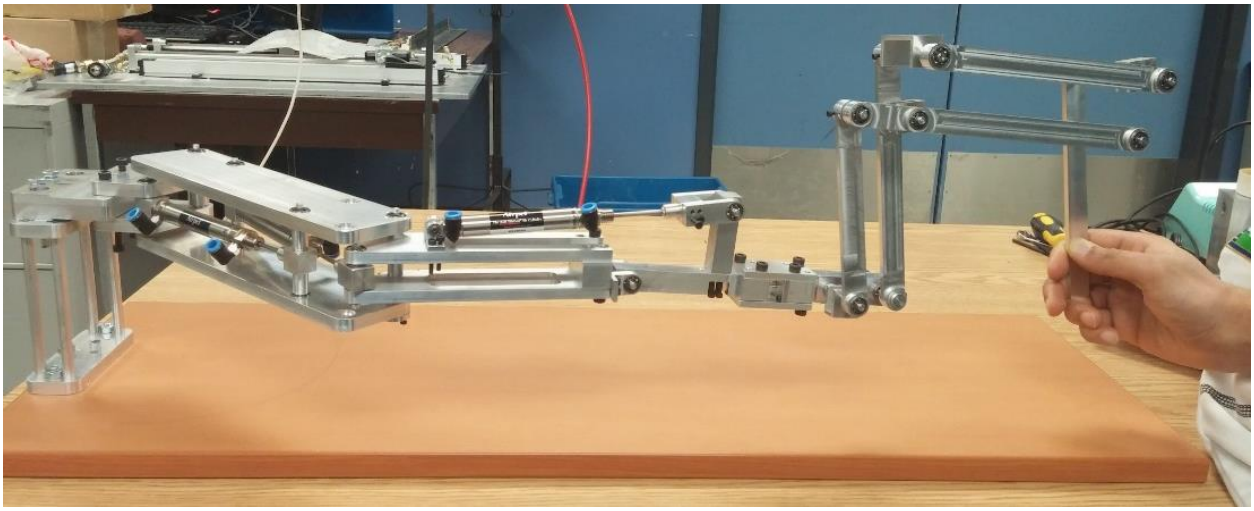

(b)

Fig. 27. Fifth manipulator device: (a) fifth device design; (b) second prototype device.

The second prototype, shown in Fig. 27, fulfills all the design criteria. Moreover, it is designed to be as small as possible. This means that it occupies less space in comparison to other models.

As shown in Fig. 27, all joints are revolute. The first three DOFs are defining the end-effector's position; however, the last two DOFs only change the end-effector's orientation and have no effect

on end-effector's position. Therefore, to calculate the position of the end-effector, the first three joints are considered in calculations.

In order to calculate the end-effector position, the transformation from the end-effector frame to the global frame is required as follows:

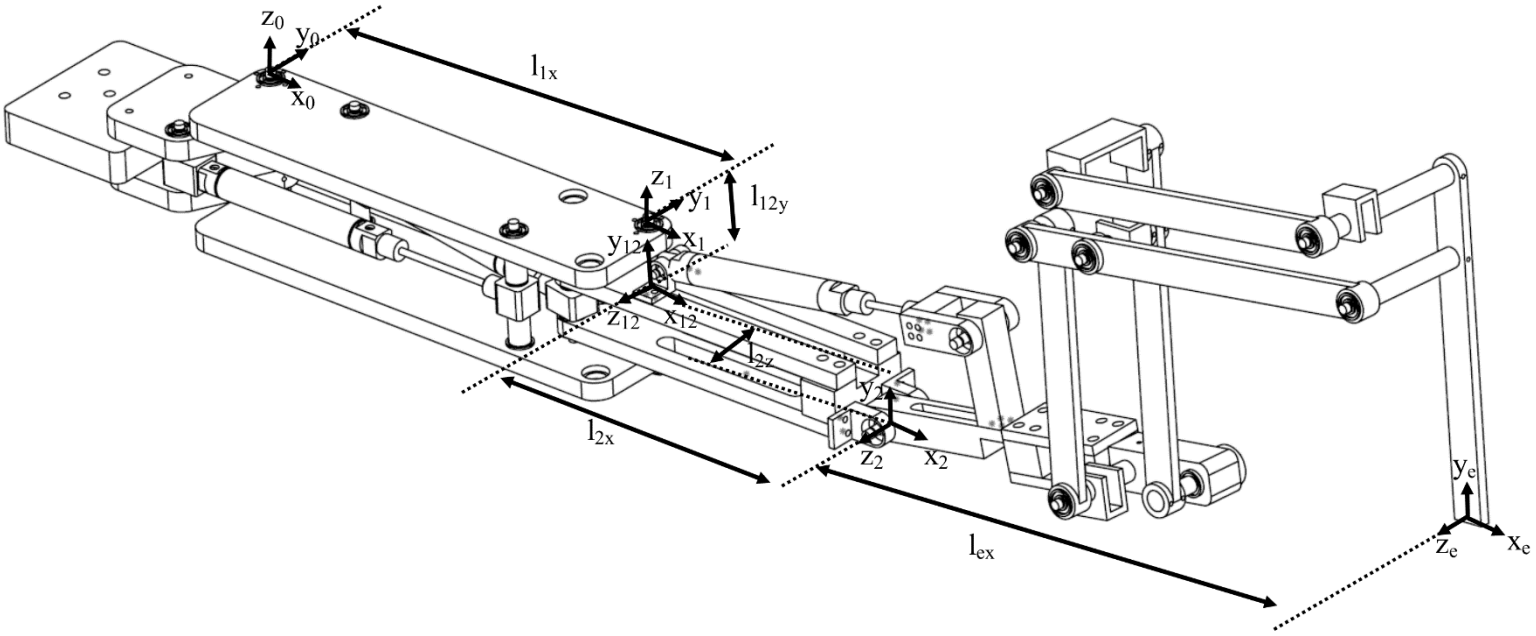

Fig. 28. Frame specification of the fifth manipulator design.

$$^{0}r_{end-effector} = {}^{0}T_{e}\,{}^{e}r_{end-effector} \tag{3.91}$$

where ${}^{e}r_{end-effector}$ describes the end-effector position with respect to the end-effector frame and ${}^{0}r_{end-effector}$ describes the position of the end-effector with respect to the global frame. Denavit-Hartenberg convention is used to derive the transformation matrix. Denavit-Hartenberg Table is calculated as follows:

Table 2: Denavit-Hartenberg parameters of the second prototype.

#	$\boldsymbol{\theta_i}$	$\boldsymbol{d_i}$	$\boldsymbol{a_i}$	$\boldsymbol{\alpha_i}$
$0-1$	θ_1	0	l_{1x}	0
$1-12$	θ_2	l_{12y}	0	$\frac{\pi}{2}$
$12-2$	0	l_{2z}	l_{2x}	0
$2-e$	θ_3	0	l_{ex}	0

The same procedure as first prototype is used to calculate the transformation matrixes, by using the parameters from Table 2. Homogenous transformation matrixes between each frames are calculated as follows:

$$ {}^{0}T_{1} = \begin{bmatrix} C\theta_1 & -S\theta_1 & 0 & l_{1x}C\theta_1 \\ S\theta_1 & C\theta_1 & 0 & l_{1x}S\theta_1 \\ 0 & 0 & 1 & 0 \\ 0 & 0 & 0 & 1 \end{bmatrix} $$

$$ {}^{1}T_{12} = \begin{bmatrix} C\theta_2 & 0 & S\theta_2 & 0 \\ S\theta_2 & 0 & -C\theta_2 & 0 \\ 0 & 1 & 0 & l_{12y} \\ 0 & 0 & 0 & 1 \end{bmatrix} $$

$$ {}^{12}T_{2} = \begin{bmatrix} 1 & 0 & 0 & l_{2x} \\ 0 & 1 & 0 & 0 \\ 0 & 0 & 1 & l_{2z} \\ 0 & 0 & 0 & 1 \end{bmatrix} $$

$$ {}^{2}T_{e} = \begin{bmatrix} C\theta_3 & -S\theta_3 & 0 & l_{ex}C\theta_3 \\ S\theta_3 & C\theta_3 & 0 & l_{ex}S\theta_3 \\ 0 & 0 & 1 & 0 \\ 0 & 0 & 0 & 1 \end{bmatrix} \tag{3.92} $$

Following equation is used to calculate the transformation matrix from the end-effector coordinate to the global coordinate.

$$ {}^{0}T_{e} = {}^{0}T_{1}\,{}^{1}T_{12}\,{}^{12}T_{2}\,{}^{2}T_{e} $$

$$ {}^{0}T_{e} = \begin{bmatrix} C\theta_1 C\theta_2 C\theta_3 - S\theta_1 S\theta_2 C\theta_3 & -C\theta_1 C\theta_2 S\theta_3 + S\theta_1 S\theta_2 S\theta_3 & C\theta_1 S\theta_2 + S\theta_1 C\theta_2 & X \\ S\theta_1 C\theta_2 C\theta_3 + C\theta_1 S\theta_2 C\theta_3 & -S\theta_1 C\theta_2 S\theta_3 - C\theta_1 S\theta_2 S\theta_3 & S\theta_1 S\theta_2 - C\theta_1 C\theta_2 & Y \\ S\theta_3 & C\theta_3 & 0 & Z \\ 0 & 0 & 0 & 1 \end{bmatrix} \quad (3.93) $$

where X, Y and Z are the end-effector positions with respect to the global frame. These positions are calculated as follows:

$$ X = l_{2z} C\theta_1 S\theta_2 + l_{ex} C\theta_1 C\theta_2 C\theta_3 + l_{2x} C\theta_1 C\theta_2 + l_{2z} S\theta_1 C\theta_2 - l_{ex} S\theta_1 S\theta_2 C\theta_3 - l_{2x} S\theta_1 S\theta_2 + l_{1x} C\theta_1 $$

$$ Y = l_{2z} S\theta_1 S\theta_2 + l_{ex} S\theta_1 C\theta_2 C\theta_3 + l_{2x} S\theta_1 C\theta_2 - l_{2z} C\theta_1 C\theta_2 + l_{ex} C\theta_1 S\theta_2 C\theta_3 + l_{2x} C\theta_1 S\theta_2 + l_{1x} S\theta_1 $$

$$ Z = l_{1x} S\theta_3 + l_{12y} \quad (3.94) $$

End-effector velocities with respect to the global frame are calculated as follows:

$$ \begin{aligned} V_x = {} & -\dot{\theta}_1 l_{2z} S\theta_1 S\theta_2 + \dot{\theta}_2 l_{2z} C\theta_1 C\theta_2 - \dot{\theta}_1 l_{ex} S\theta_1 C\theta_2 C\theta_3 - \dot{\theta}_2 l_{ex} C\theta_1 S\theta_2 C\theta_3 - \dot{\theta}_3 l_{ex} C\theta_1 C\theta_2 S\theta_3 \\ & - \dot{\theta}_1 l_{2x} S\theta_1 C\theta_2 - \dot{\theta}_2 l_{2x} C\theta_1 S\theta_2 + \dot{\theta}_1 l_{2z} C\theta_1 C\theta_2 - \dot{\theta}_2 l_{2z} S\theta_1 S\theta_2 \\ & - \dot{\theta}_1 l_{ex} C\theta_1 S\theta_2 C\theta_3 - \dot{\theta}_2 l_{ex} S\theta_1 C\theta_2 C\theta_3 + \dot{\theta}_3 l_{ex} S\theta_1 S\theta_2 S\theta_3 - \dot{\theta}_1 l_{2x} C\theta_1 S\theta_2 \\ & - \dot{\theta}_2 l_{2x} S\theta_1 C\theta_2 - \dot{\theta}_1 l_{1x} S\theta_1 \end{aligned} $$

$$V_y = \dot{\theta}_1 l_{2z} C\theta_1 S\theta_2 + \dot{\theta}_2 l_{2z} S\theta_1 C\theta_2 + \dot{\theta}_1 l_{ex} C\theta_1 C\theta_2 C\theta_3 - \dot{\theta}_2 l_{ex} S\theta_1 S\theta_2 C\theta_3 - \dot{\theta}_3 l_{ex} S\theta_1 C\theta_2 S\theta_3$$
$$+ \dot{\theta}_1 l_{2x} C\theta_1 C\theta_2 - \dot{\theta}_2 l_{2x} S\theta_1 S\theta_2 + \dot{\theta}_1 l_{2z} S\theta_1 C\theta_2 + \dot{\theta}_2 l_{2z} C\theta_1 S\theta_2$$
$$- \dot{\theta}_1 l_{ex} S\theta_1 S\theta_2 C\theta_3 + \dot{\theta}_2 l_{ex} C\theta_1 C\theta_2 C\theta_3 - \dot{\theta}_3 l_{ex} C\theta_1 S\theta_2 S\theta_3 - \dot{\theta}_1 l_{2x} S\theta_1 S\theta_2$$
$$+ \dot{\theta}_2 l_{2x} C\theta_1 C\theta_2 + \dot{\theta}_1 l_{1x} C\theta_1$$

$$V_z = \dot{\theta}_3 l_{ez} C\theta_3 \tag{3.95}$$

Jacobian matrix relates the workspace and joint space variables as follows:

$$\begin{bmatrix} V_x \\ V_y \\ V_z \end{bmatrix} = J \begin{bmatrix} \dot{\theta}_1 \\ \dot{\theta}_2 \\ \dot{\theta}_3 \end{bmatrix} \tag{3.96}$$

where J is calculated as follows:

$$J = \begin{bmatrix} J_{11} & J_{12} & J_{13} \\ J_{21} & J_{22} & J_{23} \\ 0 & 0 & J_{33} \end{bmatrix} \tag{3.97}$$

$$J_{11} = -l_{2z} S\theta_1 S\theta_2 - l_{ex} S\theta_1 C\theta_2 C\theta_3 - l_{2x} S\theta_1 C\theta_2 + l_{2z} C\theta_1 C\theta_2 - l_{ex} C\theta_1 S\theta_2 C\theta_3 - l_{2x} C\theta_1 S\theta_2$$
$$- l_{1x} S\theta_1$$

$$J_{12} = l_{2z} C\theta_1 C\theta_2 - l_{ex} C\theta_1 S\theta_2 C\theta_3 - l_{2x} C\theta_1 S\theta_2 - l_{2z} S\theta_1 S\theta_2 - l_{ex} S\theta_1 C\theta_2 C\theta_3 - l_{2x} S\theta_1 C\theta_2$$

$$J_{13} = -l_{ex} C\theta_1 C\theta_2 S\theta_3 + l_{ex} S\theta_1 S\theta_2 S\theta_3$$

$$J_{21} = l_{2z} C\theta_1 S\theta_2 + l_{ex} C\theta_1 C\theta_2 C\theta_3 + l_{2x} C\theta_1 C\theta_2 + l_{2z} S\theta_1 C\theta_2 + -l_{ex} S\theta_1 S\theta_2 C\theta_3 - l_{2x} S\theta_1 S\theta_2$$
$$+ l_{1x} C\theta_1$$

$$J_{22} = +l_{2z} S\theta_1 C\theta_2 - l_{ex} S\theta_1 S\theta_2 C\theta_3 - l_{2x} S\theta_1 S\theta_2 + l_{2z} C\theta_1 S\theta_2 + l_{ex} C\theta_1 C\theta_2 C\theta_3 + l_{2x} C\theta_1 C\theta_2$$

$$J_{23} = -l_{ex} S\theta_1 C\theta_2 S\theta_3 - l_{ex} C\theta_1 S\theta_2 S\theta_3$$

$$J_{33} = l_{ex}C\theta_3$$

After the completion of kinematic and geometric analysis for this model, a prototype was made. This prototype was fully operational and capable of mounting actuators. The second manufactured prototype has been shown to be more effective for interaction in comparison to the first prototype. It operates smoothly and is able to mount the actuator inside the links. This prototype is designed to build using Aluminum alloy, and to use the *M16D100.0U* pneumatic actuator. Moreover, it was made at the machine shop using CNC machine. As mentioned before there are other possible options for the actuator. This could also help to make some improvements in the device size and weight. Acrylic is lighter than Aluminum and it is also machinable. Additionally, *M16* actuators have shorter strokes. *M9D12.5U* is the shortest stroke pneumatic actuator of *M9* family that is commercially available. It has 12.5 mm stoke. Although using such material and actuator shrinks the device size, it also decreases the workspace.

3.2.3. Third Prototype

The third and final design was generated using Acrylic and *M16D12.5U* pneumatic actuator. Acrylic is machinable. This means that for the fabrication process CNC, manual milling and lathe machining can be used; however, the most desirable fabrication process for this application using acrylic was laser-cutting. This is because of the fact that laser-cutting is much faster and cheaper in comparison to other available manufacturing technologies. Fig. 29 shows the Final design.

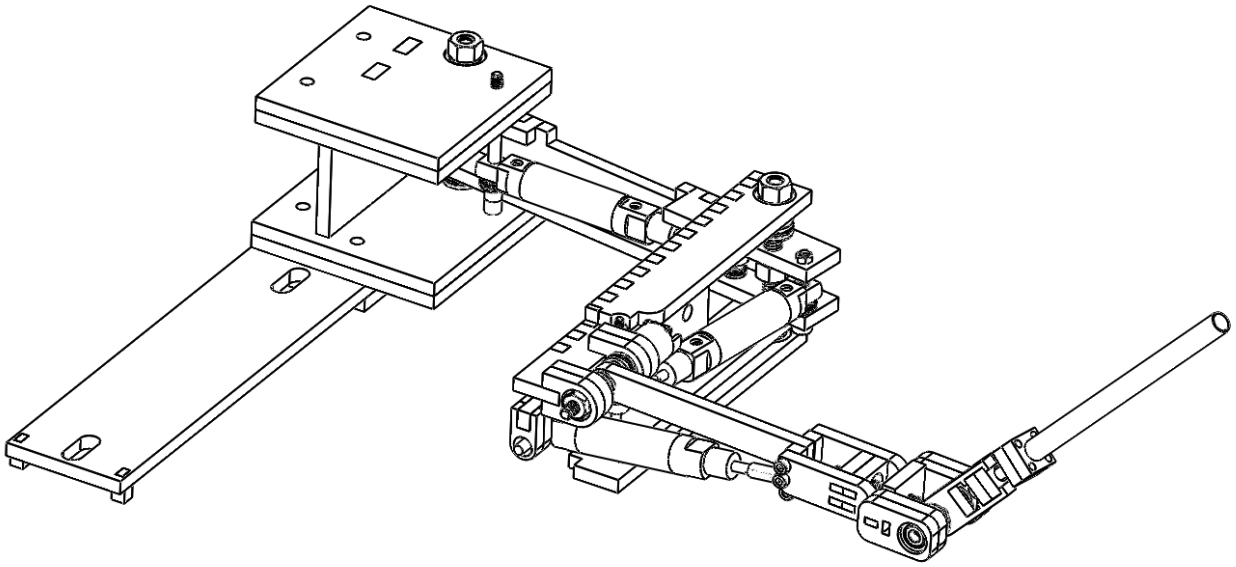

(a)

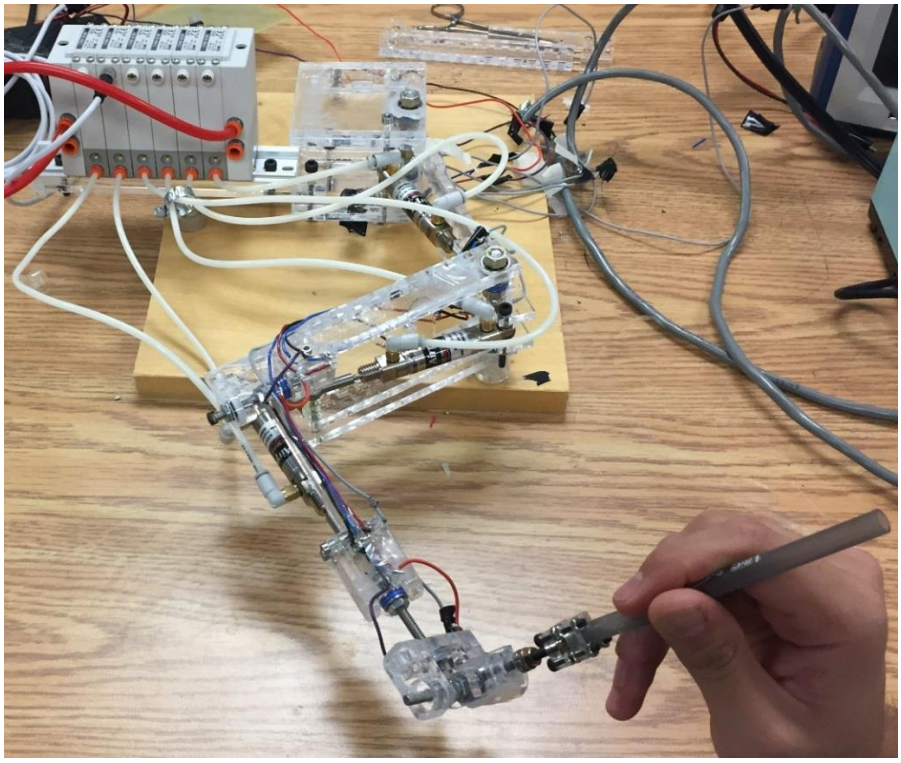

(b)

Fig. 29. Final manipulator device: (a) final device design; (b) final prototype device.

As shown in Fig. 29, the Final design has 6-DOF. All of the joints in final design are revolute. The first 3-DOFs define the end-effector's position. Furthermore, the last 3-DOFs change the end-effector's orientation and have no effect on its position. This means that end-effector's position and orientation are decoupled.

To simplify the kinematic analysis the sixth DOF is eliminated from the model. This is because of the fact that it has no effect on end-effector's position and it only changes one orientation angle. This change in orientation can be added by multiplying the rotation matrixes from the sixth DOF to the calculated rotation matrix for the first 5-DOFs.

The following figure shows the frame specifications of the Final design required to start the kinematic analysis.

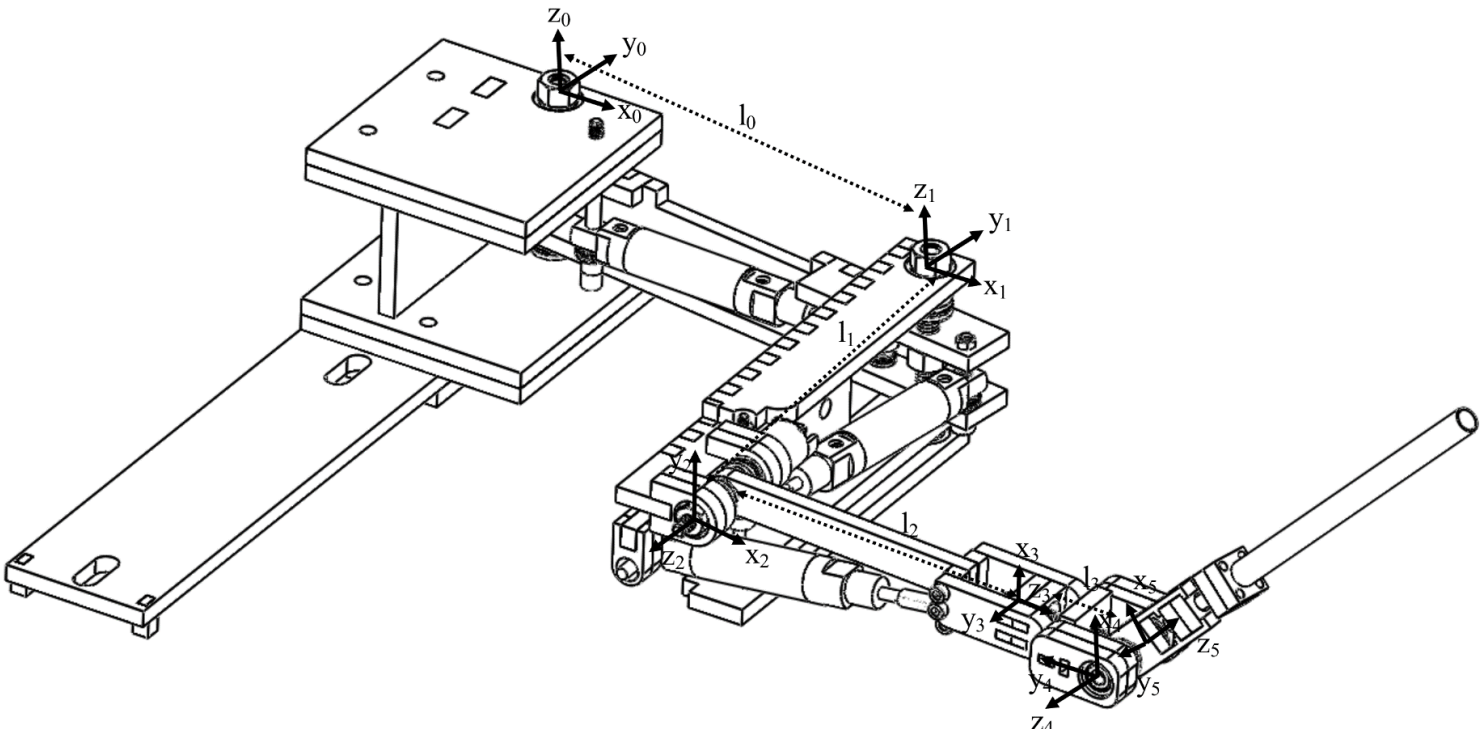

Fig. 30. Frame specification of the final manipulator design

Based on the Fig. 30, Denavit-Hartenberg table is calculated as follows:

Table 3. Denavit-Hatenberg parameter of the final prototype.

#	$\boldsymbol{\theta_i}$	$\boldsymbol{d_i}$	$\boldsymbol{a_i}$	$\boldsymbol{\alpha_i}$
$0-1$	θ_1	0	l_0	0
$1-12$	θ_2	0	0	$\frac{\pi}{2}$
$12-2$	0	l_1	0	0
$2-23$	$\theta_3+\frac{\pi}{2}$	0	0	$\frac{\pi}{2}$
$23-3$	0	l_2	0	0
$3-4$	θ_4	l_3	0	$-\frac{\pi}{2}$
$4-5$	θ_5	0	0	0

Table 3 provides the necessary information to start the kinematic calculations. These calculations followed the same procedure as first introduced for the first prototype. Homogenous transformation matrixes between each frames were calculated as follows:

$$ {}^{0}T_{1} = \begin{bmatrix} C\theta_1 & -S\theta_1 & 0 & l_0C\theta_1 \\ S\theta_1 & C\theta_1 & 0 & l_0S\theta_1 \\ 0 & 0 & 1 & 0 \\ 0 & 0 & 0 & 1 \end{bmatrix} $$

$$ {}^{1}T_{12} = \begin{bmatrix} C\theta_2 & 0 & S\theta_2 & 0 \\ S\theta_2 & 0 & -C\theta_2 & 0 \\ 0 & 1 & 0 & 0 \\ 0 & 0 & 0 & 1 \end{bmatrix} $$

$$^{12}T_2 = \begin{bmatrix} 1 & 0 & 0 & 0 \\ 0 & 1 & 0 & 0 \\ 0 & 0 & 1 & l_1 \\ 0 & 0 & 0 & 1 \end{bmatrix}$$

$$^{2}T_{23} = \begin{bmatrix} -S\theta_3 & 0 & C\theta_3 & 0 \\ C\theta_3 & 0 & S\theta_3 & 0 \\ 0 & 1 & 0 & 0 \\ 0 & 0 & 0 & 1 \end{bmatrix}$$

$$^{23}T_3 = \begin{bmatrix} 1 & 0 & 0 & 0 \\ 0 & 1 & 0 & 0 \\ 0 & 0 & 1 & l_2 \\ 0 & 0 & 0 & 1 \end{bmatrix}$$

$$^{3}T_4 = \begin{bmatrix} C\theta_4 & 0 & -S\theta_4 & 0 \\ S\theta_4 & 0 & C\theta_4 & 0 \\ 0 & -1 & 0 & l_3 \\ 0 & 0 & 0 & 1 \end{bmatrix}$$

$$^{4}T_5 = \begin{bmatrix} C\theta_1 & -S\theta_1 & 0 & 0 \\ S\theta_1 & C\theta_1 & 0 & 0 \\ 0 & 0 & 1 & 0 \\ 0 & 0 & 0 & 1 \end{bmatrix} \quad (3.98)$$

In order to calculate the end-effector's position and orientation, a sequence of transformation matrixes were used as follows:

$$^{0}r_5 = {}^{0}T_5 \, {}^{5}r_5$$

$$^{0}T_e = {}^{0}T_1 \, {}^{1}T_{12} \, {}^{12}T_2 \, {}^{2}T_e$$

$$^{0}T_e = \begin{bmatrix} R_{11} & R_{12} & R_{13} & X \\ R_{21} & R_{22} & R_{23} & Y \\ R_{31} & R_{32} & R_{33} & Z \\ 0 & 0 & 0 & 1 \end{bmatrix} \quad (3.99)$$

Where R is the rotation matrix, and X, Y and Z are the end-effector's position with respect to the global frame. Rotation Matrix is calculated as follows:

$$R_{11} = -C\theta_1 C\theta_2 S\theta_3 C\theta_4 C\theta_5 - C\theta_1 C\theta_2 C\theta_3 S\theta_5 + C\theta_1 S\theta_2 S\theta_4 C\theta_5 + S\theta_1 S\theta_2 S\theta_3 C\theta_4 C\theta_5 + S\theta_1 S\theta_2 C\theta_3 S\theta_5 + S\theta_1 C\theta_2 S\theta_4 C\theta_5$$

$$R_{12} = C\theta_1 C\theta_2 S\theta_3 C\theta_4 S\theta_5 - C\theta_1 C\theta_2 C\theta_3 C\theta_5 - C\theta_1 S\theta_2 S\theta_4 S\theta_5 - S\theta_1 S\theta_2 S\theta_3 C\theta_4 S\theta_5 + S\theta_1 S\theta_2 C\theta_3 C\theta_5 - S\theta_1 C\theta_2 S\theta_4 S\theta_5$$

$$R_{13} = C\theta_1 C\theta_2 S\theta_3 S\theta_4 + C\theta_1 S\theta_2 C\theta_4 - S\theta_1 S\theta_2 S\theta_3 S\theta_4 + S\theta_1 C\theta_2 C\theta_4$$

$$R_{21} = -S\theta_1 C\theta_2 S\theta_3 C\theta_4 C\theta_5 - S\theta_1 C\theta_2 C\theta_3 S\theta_5 + S\theta_1 S\theta_2 S\theta_4 C\theta_5 - C\theta_1 S\theta_2 S\theta_3 C\theta_4 C\theta_5 - C\theta_1 S\theta_2 S\theta_3 C\theta_4 C\theta_5 - C\theta_1 S\theta_2 C\theta_3 S\theta_5 - C\theta_1 C\theta_2 S\theta_4 C\theta_5$$

$$R_{22} = S\theta_1 C\theta_2 S\theta_3 C\theta_4 S\theta_5 - S\theta_1 C\theta_2 C\theta_3 C\theta_5 - S\theta_1 S\theta_2 S\theta_4 S\theta_5 + C\theta_1 S\theta_2 S\theta_3 C\theta_4 S\theta_5 - C\theta_1 S\theta_2 C\theta_3 C\theta_5 + C\theta_1 C\theta_2 S\theta_4 C\theta_5$$

$$R_{23} = S\theta_1 C\theta_2 S\theta_3 S\theta_4 + S\theta_1 S\theta_2 C\theta_4 + C\theta_1 S\theta_2 S\theta_3 S\theta_4 - C\theta_1 C\theta_2 C\theta_4$$

$$R_{31} = C\theta_3 C\theta_4 C\theta_5 - S\theta_3 S\theta_5$$

$$R_{32} = -C\theta_3 C\theta_4 S\theta_5 - S\theta_3 C\theta_5$$

$$R_{33} = -C\theta_3 S\theta_4 \tag{3.100}$$

X, Y and Z positions were calculated as follows:

$$X = l_0 C\theta_1 + l_1 C\theta_1 S\theta_2 + l_1 S\theta_1 C\theta_2 + (l_2 + l_3) C\theta_1 C\theta_2 C\theta_3 - (l_2 + l_3) S\theta_1 S\theta_2 S\theta_3$$

$$Y = l_0 S\theta_1 + l_1 S\theta_1 S\theta_2 - l_1 C\theta_1 C\theta_2 + (l_2 + l_3) S\theta_1 C\theta_2 C\theta_3 + (l_2 + l_3) C\theta_1 S\theta_2 S\theta_3$$

$$Z = (l_2 + l_3) S\theta_3 \tag{3.101}$$

The workspace for the final prototype is shown in Fig. 31. As shown In Fig. 31, the maximum cube size that could fit inside the work space has 80 mm length.

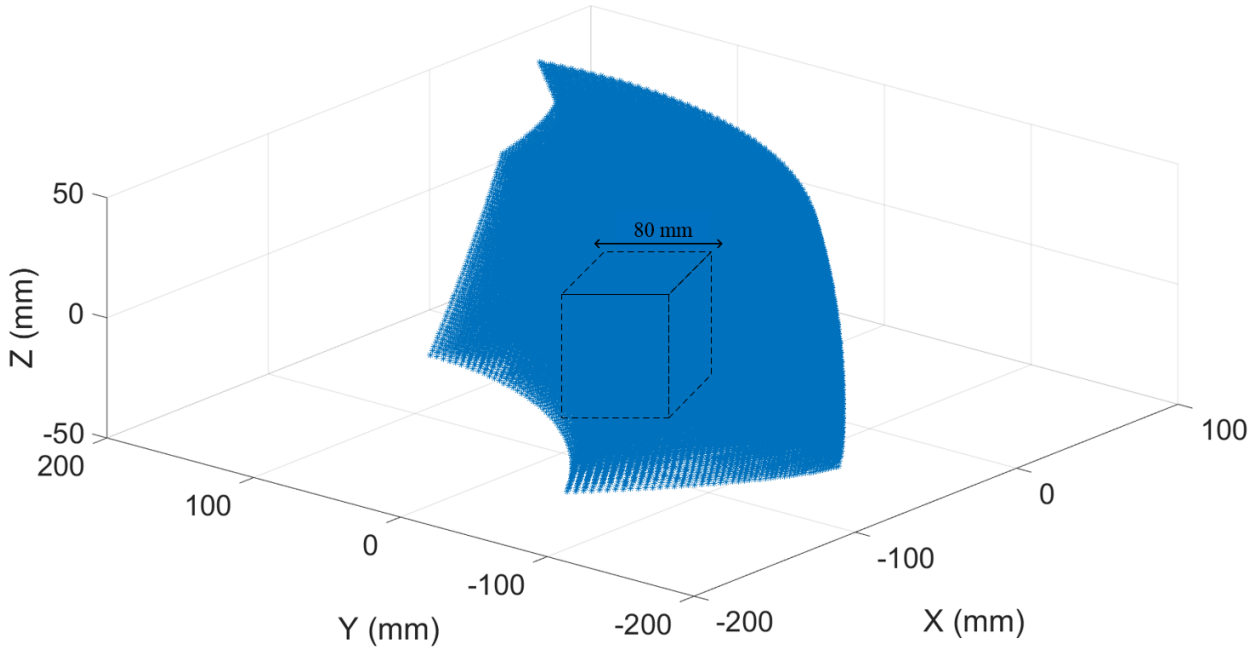

Fig. 31. 3D workspace of the final prototype.

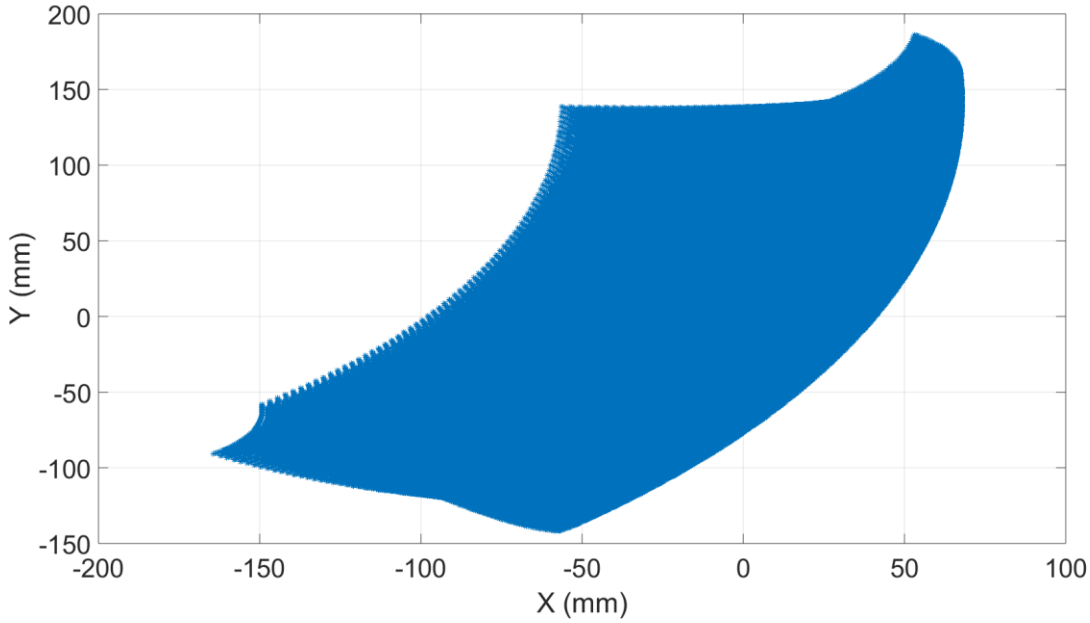

Fig. 32. Workspace of the final prototype, XY plane.

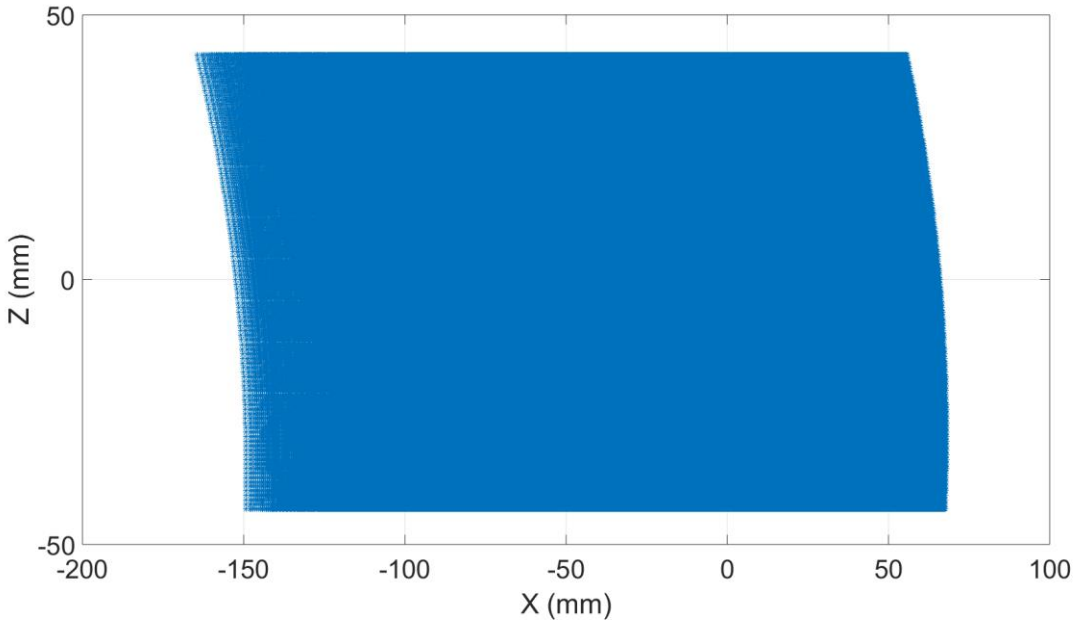

Fig. 33. Workspace of the final prototype, XZ plane.

End-effector velocities with respect to the global frame were calculated as follows. Global velocity equations were derived from the global positions by taking derivative with respect to time.

$$V_x = -l_0\dot{\theta}_1 S\theta_1 + l_1(\dot{\theta}_1 + \dot{\theta}_2)C\theta_{12} - (l_2 + l_3)(\dot{\theta}_1 S\theta_1 C\theta_2 C\theta_3 + \dot{\theta}_2 C\theta_1 S\theta_2 C\theta_3 + \dot{\theta}_3 C\theta_1 C\theta_2 S\theta_3) - (l_2 + l_3)(\dot{\theta}_1 C\theta_1 S\theta_2 S\theta_3 + \dot{\theta}_2 S\theta_1 C\theta_2 S\theta_3 + \dot{\theta}_3 S\theta_1 S\theta_2 C\theta_3)$$

$$V_y = l_0\dot{\theta}_1 C\theta_1 + l_1(\dot{\theta}_1 + \dot{\theta}_2)S\theta_{12} + (l_2 + l_3)(\dot{\theta}_1 C\theta_1 C\theta_2 C\theta_3 - \dot{\theta}_2 S\theta_1 S\theta_2 C\theta_3 - \dot{\theta}_3 S\theta_1 C\theta_2 S\theta_3) + (l_2 + l_3)(-\dot{\theta}_1 S\theta_1 S\theta_2 S\theta_3 + \dot{\theta}_2 C\theta_1 C\theta_2 S\theta_3 + \dot{\theta}_3 C\theta_1 S\theta_2 C\theta_3)$$

$$V_z = \dot{\theta}_3(l_2 + l_3)C\theta_3 \tag{3.102}$$

Jacobian matrix relates the workspace and joint space variables as follows:

$$\begin{bmatrix} V_x \\ V_y \\ V_z \end{bmatrix} = J_{3\times5} \begin{bmatrix} \dot{\theta}_1 \\ \dot{\theta}_2 \\ \dot{\theta}_3 \\ \dot{\theta}_4 \\ \dot{\theta}_5 \end{bmatrix} \tag{3.103}$$

where J is calculated as follows:

$$J = \begin{bmatrix} J_{11} & J_{12} & J_{13} & 0 & 0 \\ J_{21} & J_{22} & J_{23} & 0 & 0 \\ 0 & 0 & J_{33} & 0 & 0 \end{bmatrix} \tag{3.104}$$

$$J_{11} = -l_0 S\theta_1 + l_1 C\theta_{12} - (l_2 + l_3)(S\theta_1 C\theta_2 C\theta_3 + C\theta_1 S\theta_2 S\theta_3)$$

$$J_{12} = l_1 C\theta_{12} - (l_2 + l_3)(C\theta_1 S\theta_2 C\theta_3) - (l_2 + l_3)(S\theta_1 C\theta_2 S\theta_3)$$

$$J_{13} = -(l_2 + l_3)(C\theta_1 C\theta_2 S\theta_3 + S\theta_1 S\theta_2 C\theta_3)$$

$$J_{21} = l_0 C\theta_1 + l_1 S\theta_{12} + (l_2 + l_3)(C\theta_1 C\theta_2 C\theta_3 - S\theta_1 S\theta_2 S\theta_3)$$

$$J_{22} = l_1 S\theta_{12} + (l_2 + l_3)(-S\theta_1 S\theta_2 C\theta_3) + (l_2 + l_3)(C\theta_1 C\theta_2 S\theta_3)$$

$$J_{23} = (l_2 + l_3)(-S\theta_1 C\theta_2 S\theta_3) + (l_2 + l_3)(C\theta_1 S\theta_2 C\theta_3)$$

$$J_{33} = (l_2 + l_3) C\theta_3$$

A quantitative measurement was introduced by Tsuneo Yoshikawa to calculate the manipulability of a device. It uses the Singular Value Decomposition (SVD) of the Jacobian matrix. For any Jacobian matrix J, there are two orthogonal matrices U and V^T such that [40]:

$$J = U\Sigma V^T \tag{3.105}$$

where Σ is a diagonal matrix with non-negative numbers as follows:

$$\Sigma = \begin{bmatrix} \sigma_1 & 0 & 0 \\ 0 & \sigma_2 & 0 \\ 0 & 0 & \sigma_3 \end{bmatrix} \tag{3.106}$$

where σ_1, σ_2 and σ_3 are the square root of the Jacobian eigenvalues. The manipulability measurement that was provided by Tsuneo Yoshikawa is as follows:

$$w = \sigma_1 \sigma_2 \sigma_3 = \sqrt{\det(J\,J^T)} \tag{3.107}$$

This measurement is illustrated for the first two rotary joints in following figure:

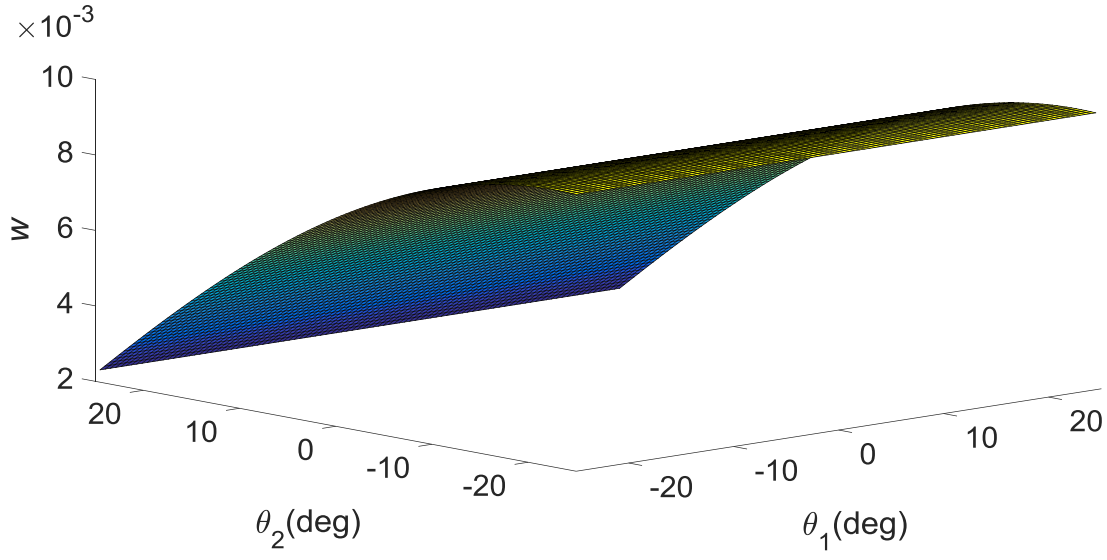

Fig. 34. Manipulability measurement.

Jacobian Matrix establishes a relationship between the joint torques and applied forces at the end-effector. This relationship is based on the principle of the virtual work. The relationship between the joint torques and the end-effector forces can be written as follows:

$$\begin{bmatrix} T_1 \\ T_2 \\ T_3 \\ T_4 \\ T_5 \end{bmatrix} = J^T \begin{bmatrix} F_x \\ F_y \\ F_z \end{bmatrix} \tag{3.109}$$

where F_x , F_y and F_z are the end-effector forces with respect to the global frame. Joint torques are calculated, using Jacobian matrix, as follows:

$$T_1 = \left(-l_0 S\theta_1 + l_1 C\theta_{12} - (l_2 + l_3)(S\theta_1 C\theta_2 C\theta_3 + C\theta_1 S\theta_2 S\theta_3)\right)F_x$$
$$+ \left(l_0 C\theta_1 + l_1 S\theta_{12} + (l_2 + l_3)(C\theta_1 C\theta_2 C\theta_3 - S\theta_1 S\theta_2 S\theta_3)\right)F_y$$

$$T_2 = \left(l_1 C\theta_{12} - (l_2 + l_3)(C\theta_1 S\theta_2 C\theta_3) - (l_2 + l_3)(S\theta_1 C\theta_2 S\theta_3)\right)F_x$$
$$+ \left(l_1 S\theta_{12} + (l_2 + l_3)(-S\theta_1 S\theta_2 C\theta_3) + (l_2 + l_3)(C\theta_1 C\theta_2 S\theta_3)\right)F_y$$

$$T_3 = \left(-(l_2 + l_3)\left(C\theta_1 C\theta_2 S\theta_3 + \dot{\theta}_3 S\theta_1 S\theta_2 C\theta_3\right)\right)F_x + \left((l_2 + l_3)(-S\theta_1 C\theta_2 S\theta_3) +\right.$$
$$\left.(l_2 + l_3)(C\theta_1 S\theta_2 C\theta_3)\right)F_y + \left((l_2 + l_3)C\theta_3\right)F_Z \quad (3.110)$$

These equations were used in order to generate the required global forces at the end-effector from the joint torques that are created by actuators. These forces were calculated based on the second environment model that haptic device is interacting with.

The equations of the Arm section are used in order to derive the relationship between the actuating force and torques created at the joints. These equations are as follows:

$$F_{act1} = \frac{T_1}{l_{2\_1}\cos(\theta_1 + \varphi_1)}$$

$$F_{act2} = \frac{-T_2}{l_{2\_2}\cos(\theta_2 - \varphi_2)}$$

$$F_{act3} = \frac{T_3}{l_{2\_3}\sin(\beta_3)} \quad (3.111)$$

A prototype of the final design has been manufactured after completion of geometric, kinematic and force analysis. This prototype is designed and manufactured to be capable of mounting actuators, valves and rotary position sensors. This prototype is illustrated in following figure.

3.3. Summary

Chapter 3 proposed design concepts to actuate the prismatic actuators. Arm geometries were calculated based on the design requirements. Then, the haptic device design was completed by using the sequence of arm assemblies. Multiple prototypes were made and the results were discussed. The final prototype has 6-DOF and three pneumatic actuators. It has the minimum of 5 cm work space cube and is made of Acrylic. Laser cutting and assembly were the only processes used to manufacture the final prototype. The final prototype was chosen as an answer to the research questions.

4. PRELIMINARY PERFORMANCE VERIFICATION

There are some instruments that are necessary to run a pneumatic actuated device. This includes the air supply, compressor, valves, transducers and control circuit. The air supply provides the air for the compressor and then the compressor pressurizes the air up to the supply pressure. Then, proportional pressure regulators use the supply pressure and the command signal that comes from the control circuit to pressurize the actuator up to a certain limit. Transducers also monitor the pressure within the actuator to give feedback to the control circuit.

The third manufactured device has three actuated degrees of freedom. *M9D12.5U* [41] pneumatic actuator, which is commercially available by *Airpel*, is used along with *ITV0030-3UMS* [42] proportional pressure regulator, made by *SMC*, to run the experiments.

Fig. 35. M9D12.5U pneumatic actuator (picture from: [43]).

Fig. 36. ITV0030-3UMS valves and manifolds (source: [42]) .

Fig. 35 shows the double acting, single rod and anti-stiction air cylinder which is used as actuator. Fig. 36 shows the proportional pressure regulators that are used to pressurize the pneumatic actuators. There are 3 pneumatic actuators required to run the experiment. Each actuator is double acting means that they should have two pressure inputs. Therefore, six proportional pressure regulator is used.

End-effector position should be calculated during the experiment. This is because of the fact that position is an input to the second environment. Rotary position sensor is attached at each joint to monitor the position of the end-effector. This sensor is shown in the following figure.

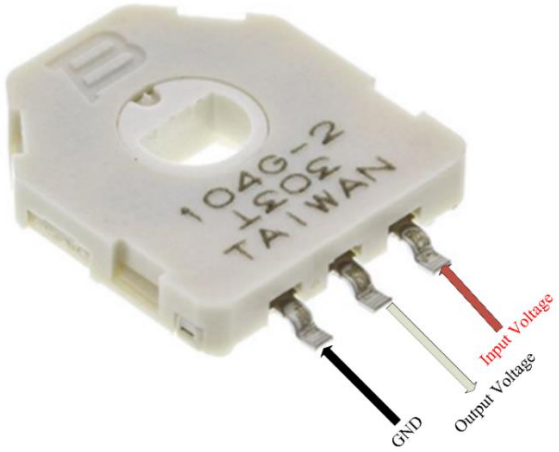

Fig. 37. Rotary position sensor.

Fig. 37 shows the 3382-12 mm rotary position sensor [44]. This sensor creates a voltage which is proportional to the shaft's rotation angle. Quanser Q8 Data Acquisition Board (DAQ) is used in order to monitor the output voltage from the rotary position sensors.

The first experiment of the haptic device was performed for about 30 seconds. End-effector's positions are calculated after monitoring the voltages and performing the calculations. During the experiment, each joint angle was moved respectively, from the first joint to the last one, to show the joint space.

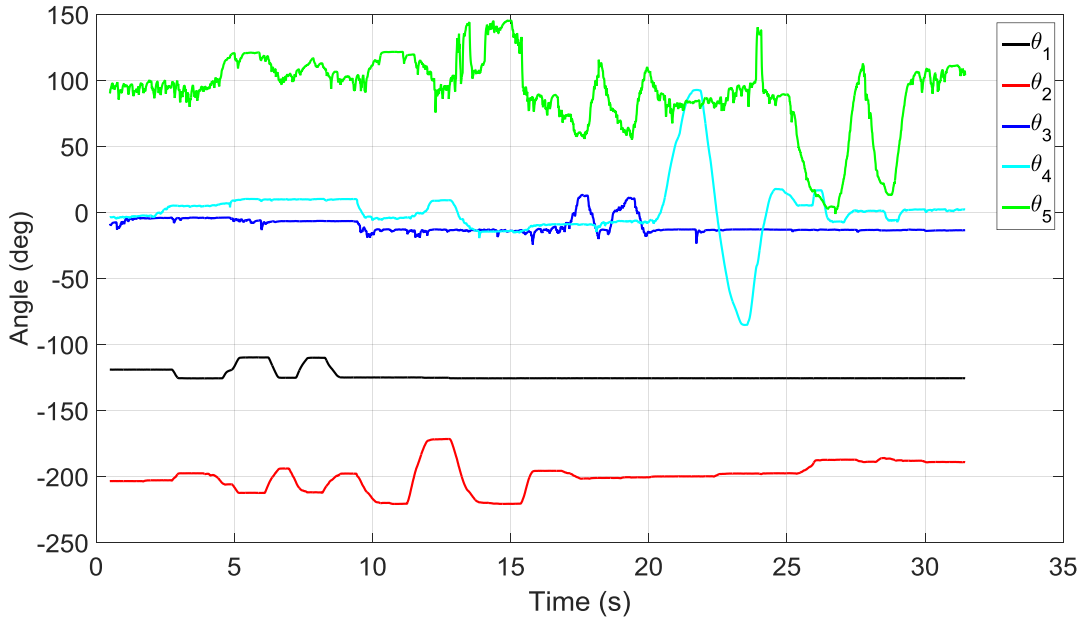

Fig. 38. Measured angles from the rotary sensors.

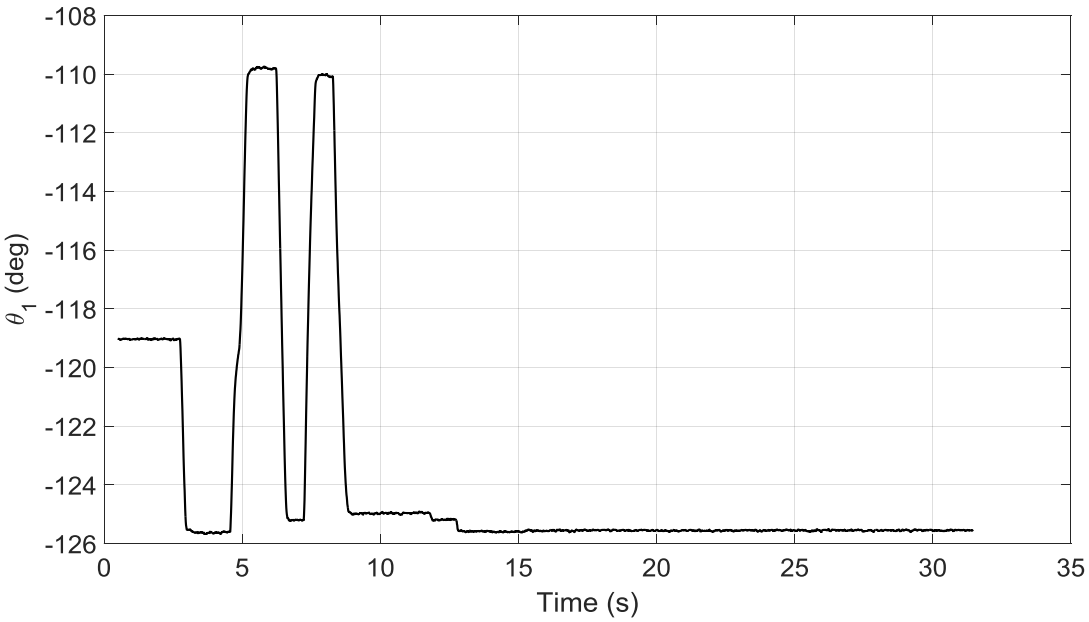

Fig. 39. First joint angle.

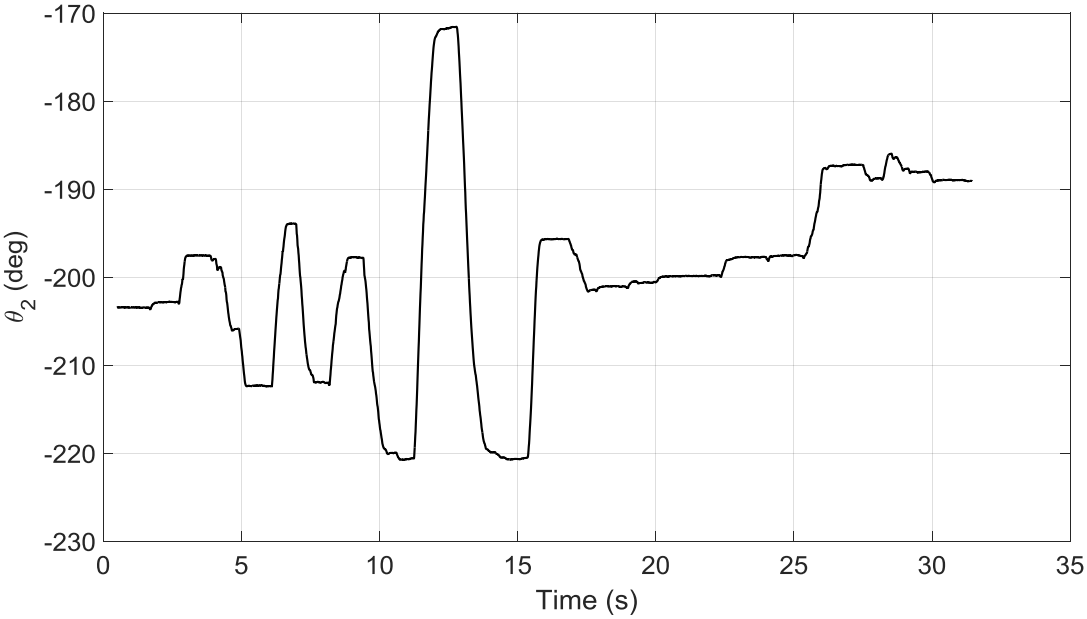

Fig. 40. Second joint angle.

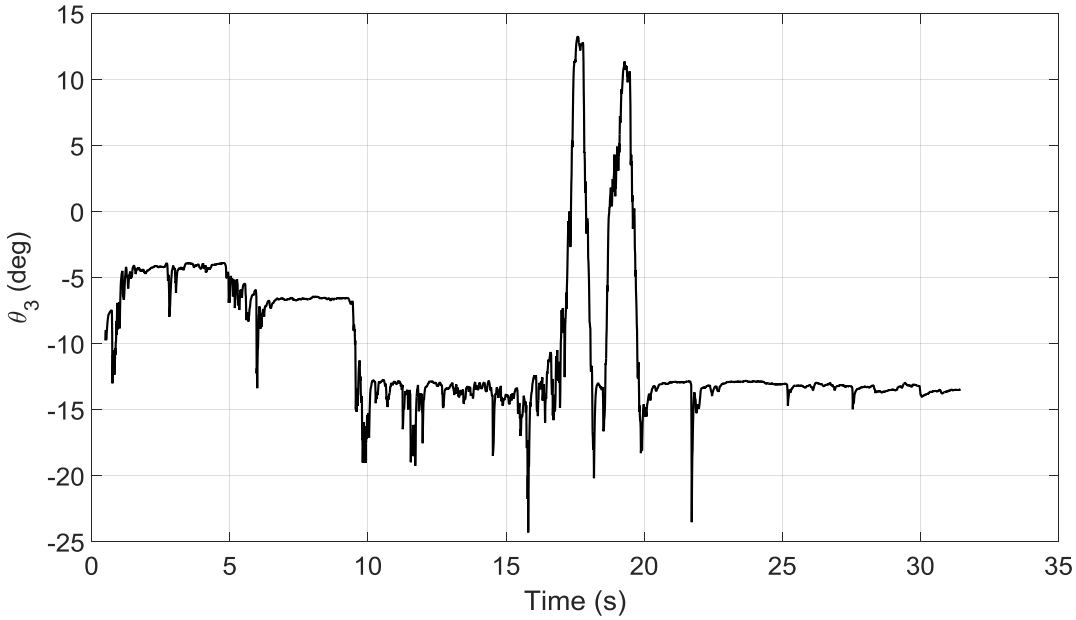

Fig. 41. Third joint angle.

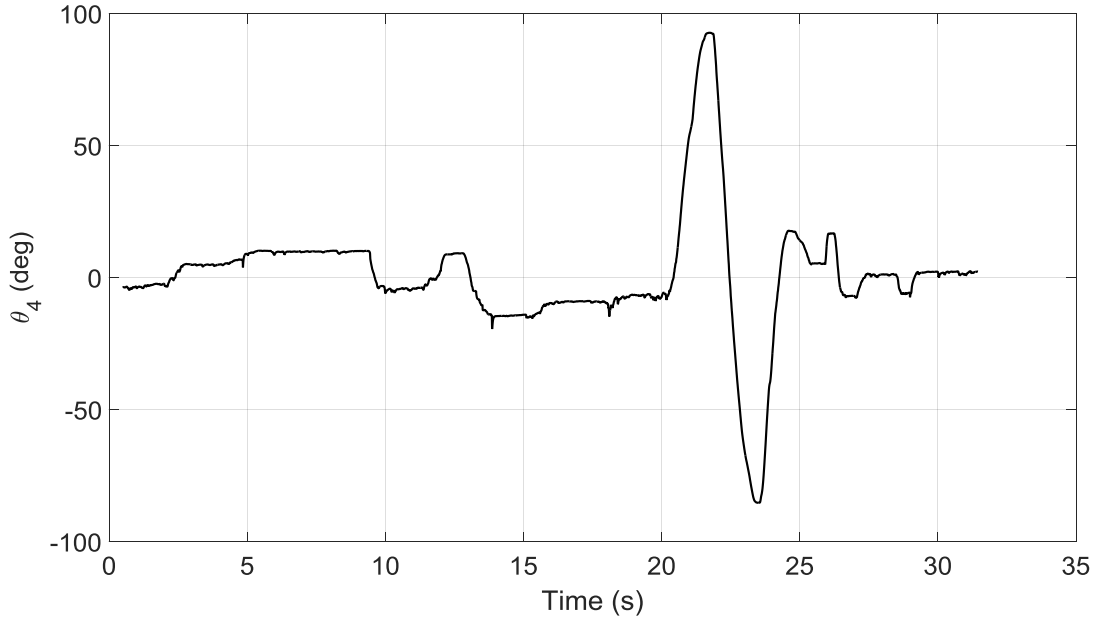

Fig. 42. Fourth joint angle.

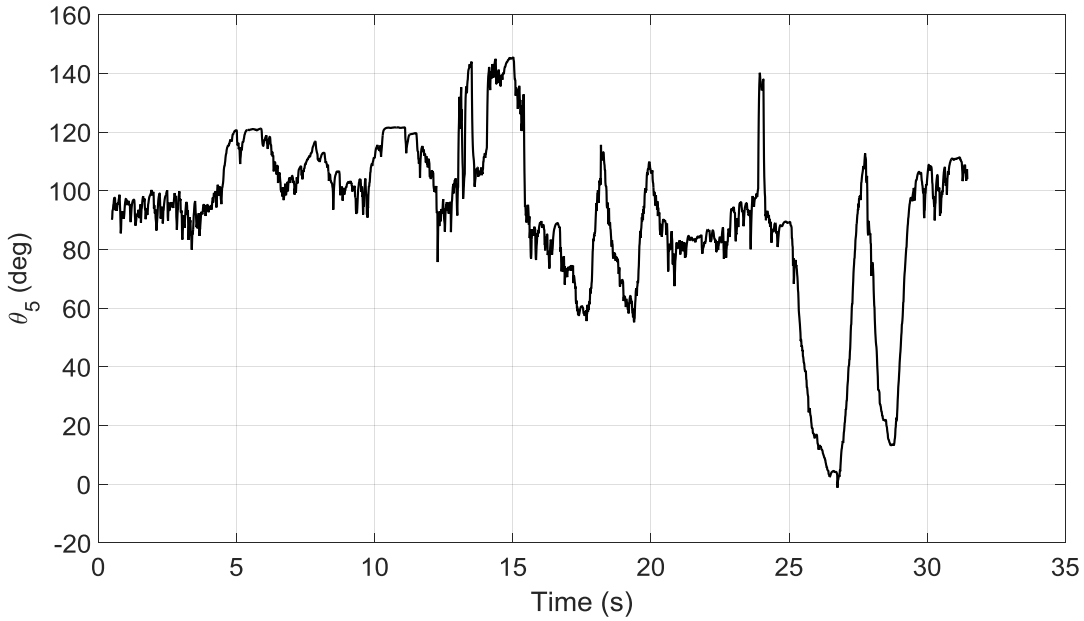

Fig. 43. Fifth joint angle.

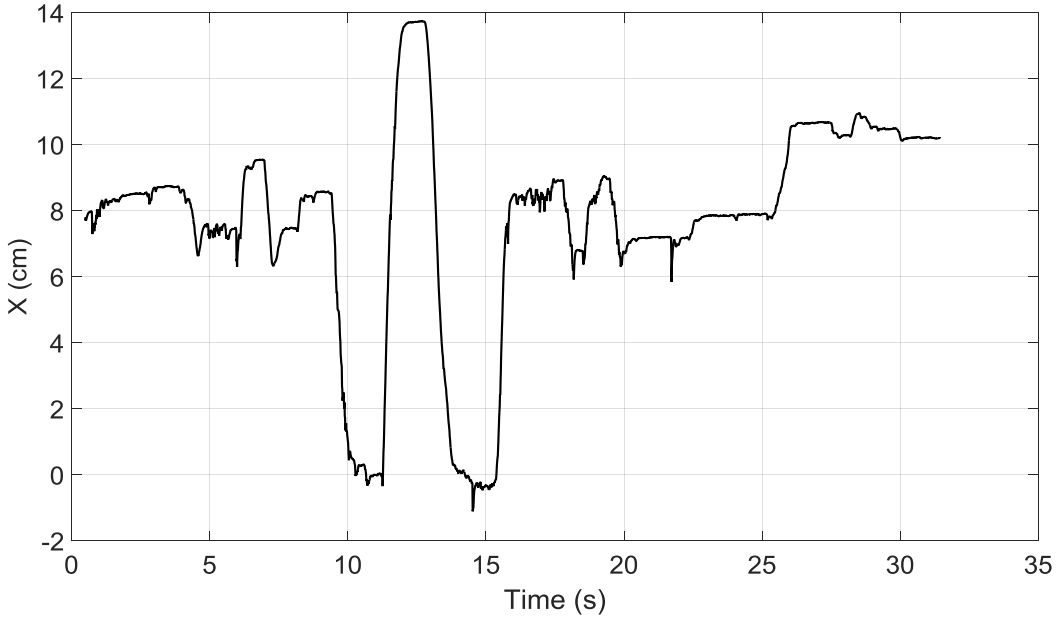

Fig. 44. *X* position of end-effector.

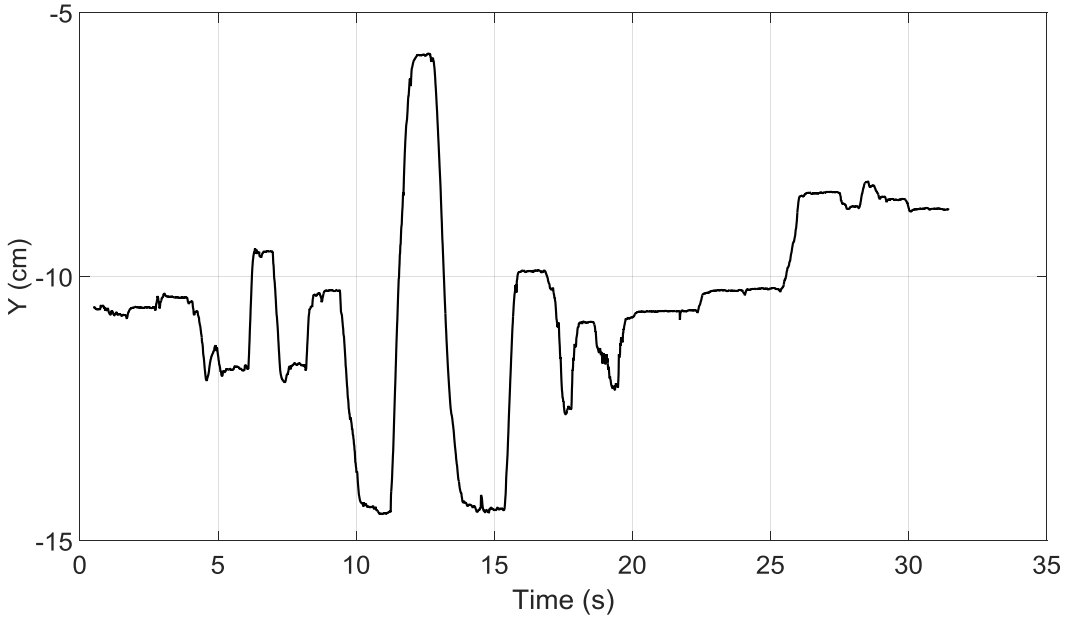

Fig. 45. *Y* position of end-effector.

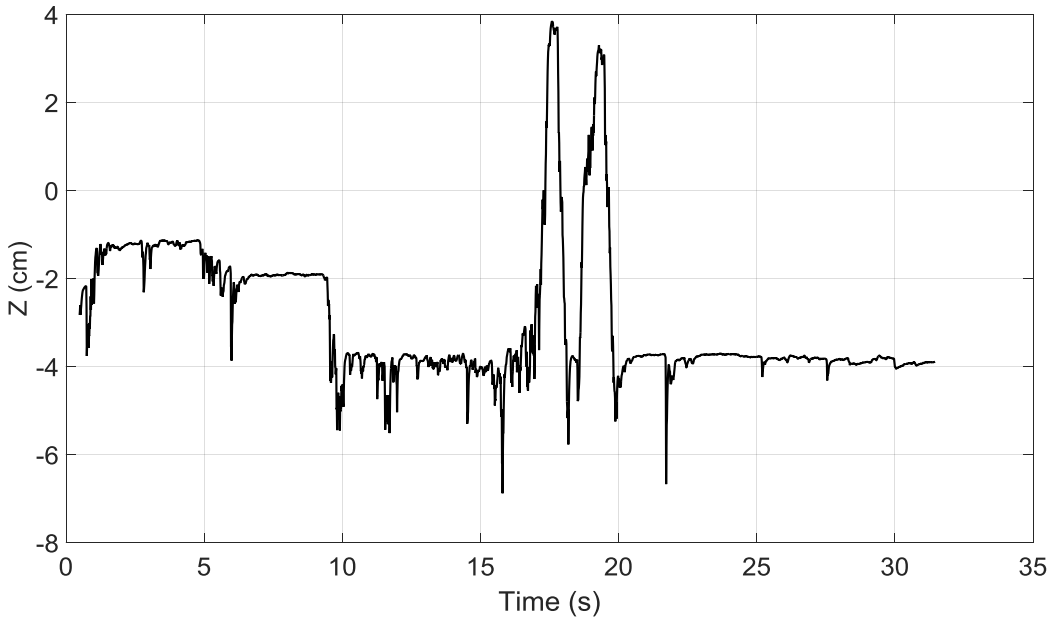

Fig. 46. *Z* position of end-effector.

Calculated positions in Fig. 44 through Fig. 46 can be used to feed into a simulated environment that the haptic device has interaction with. Therefore, a model for the simulated environment should be developed first. A simple spring model is used as follows:

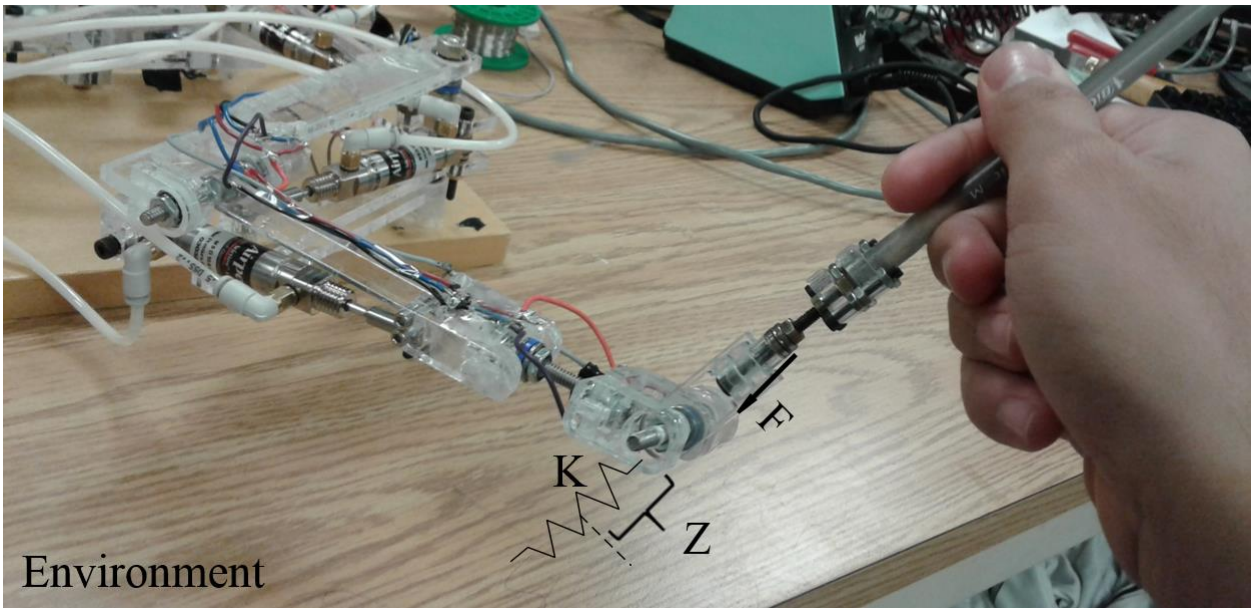

Fig. 47. Model of virtual environment.

Following equation is used to model the environment.

$$F = KZ \tag{4.3}$$

where K is the stiffness of the environment, Z is the displacement of spring and F is the force that is applied to the environment.

The second experiment is performed by giving the Z values, that are calculated from rotary position sensors output, to the simulated environment. Then, the simulated environment generates the interaction forces. These forces are given to the haptic device as required interaction forces and it creates these forces at its end-effector. The experiment results are shown in following figures.

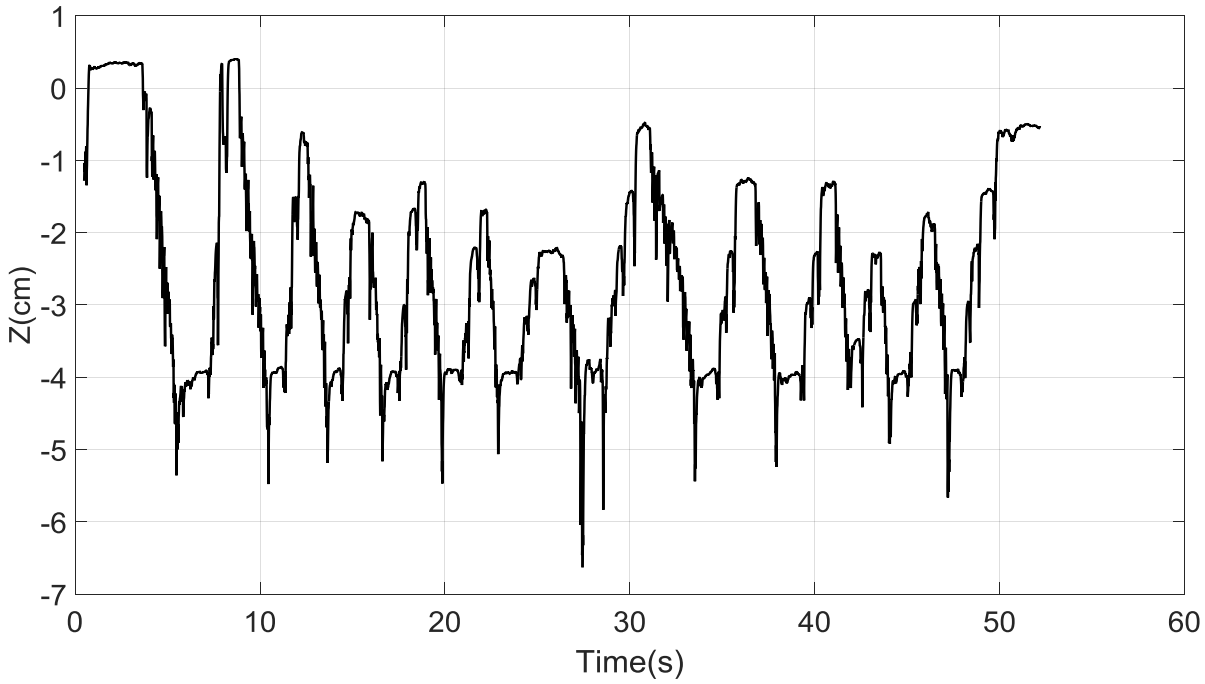

Fig. 48. Z displacement of end-effector.

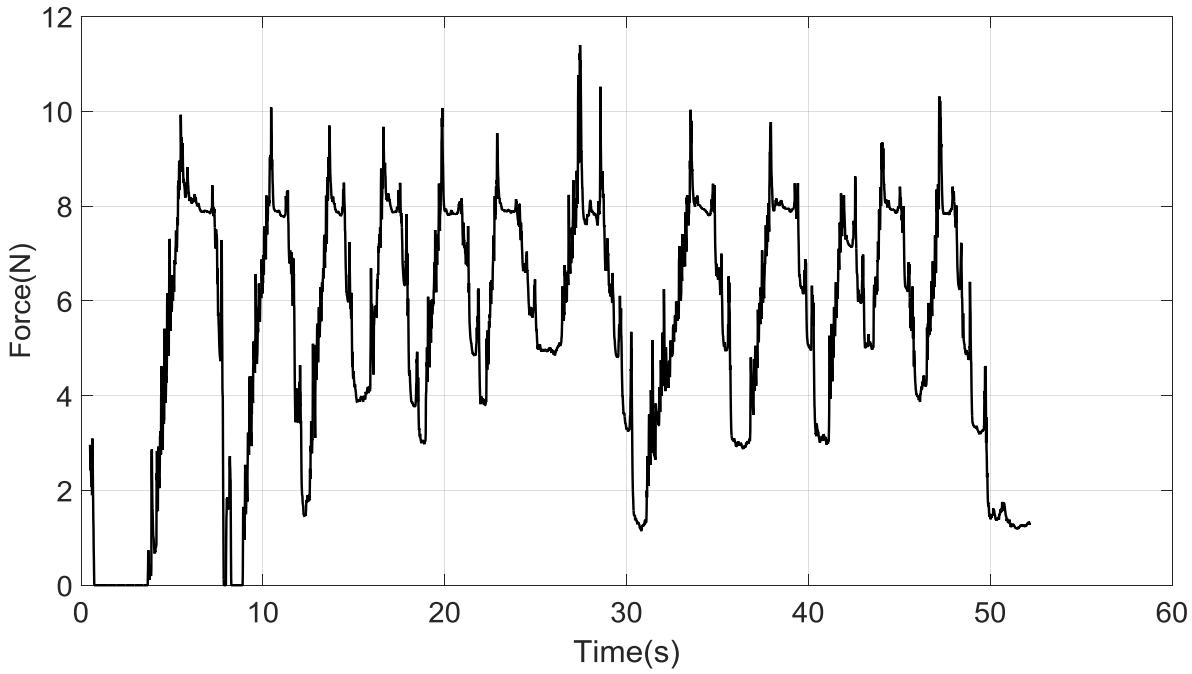

Fig. 49. Interaction force position of the end-effector.

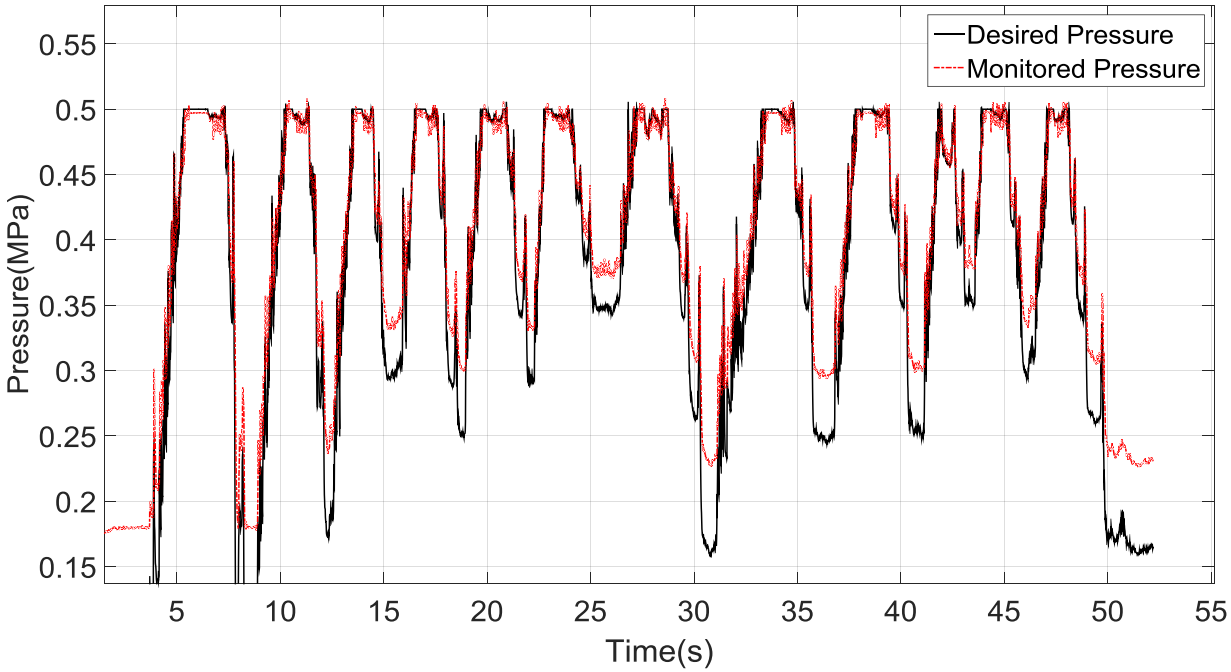

Fig. 50. Desired and monitored pressure of the third actuator.

Based on Fig. 48, the haptic device end-effector goes down several times. At the same time, as shown in Fig. 49, haptic device creates a force that is proportional to the displacement of the haptic end-effector.

The final experiment adds a limit to the end-effector's workspace. This limit is a square of 5 cm, and actuators create a constant force whenever the end-effector passes the boundaries. These boundaries are shown in following figure.

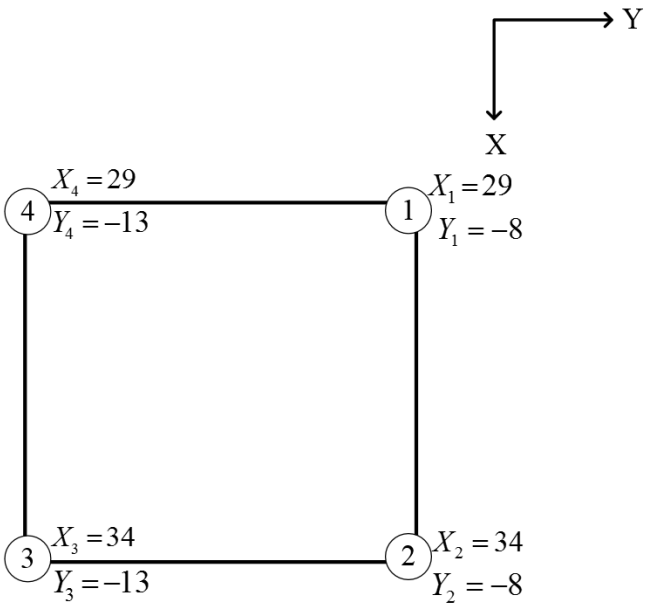

Fig. 51. End-effector's workspace boundaries.

Following figures show the X position of the end-effector, and the rear side's pressure of the second actuator.

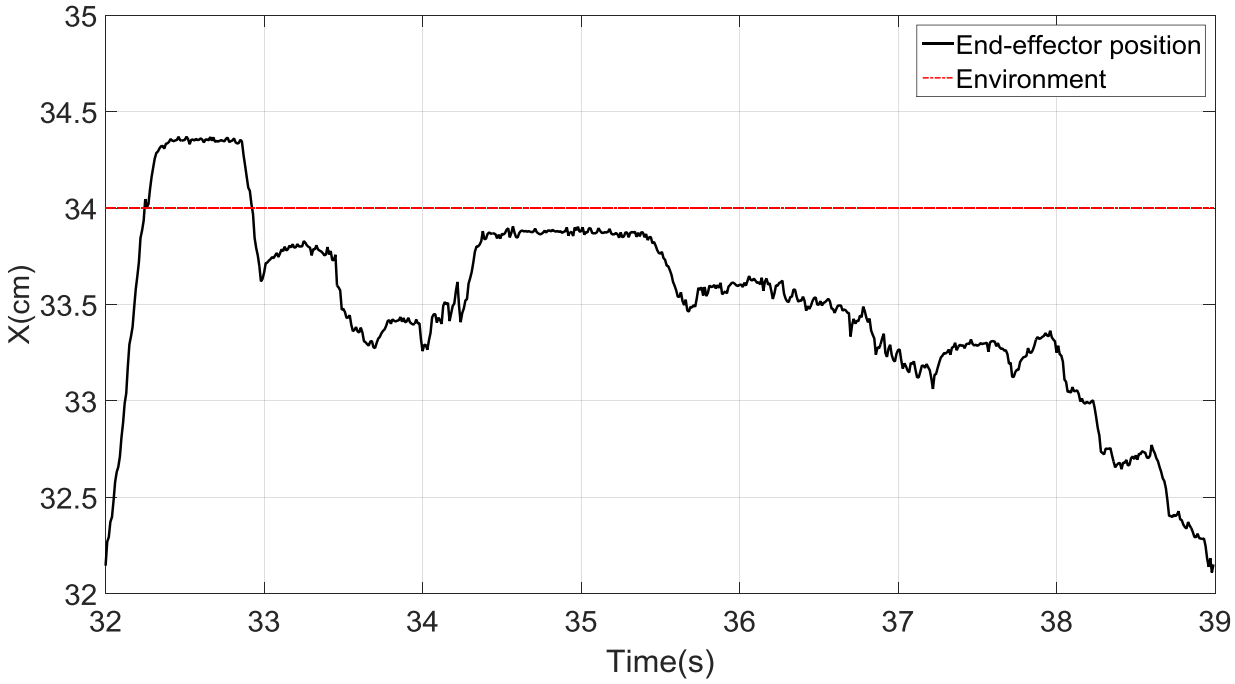

Fig. 52. *X* position of the end-effector.

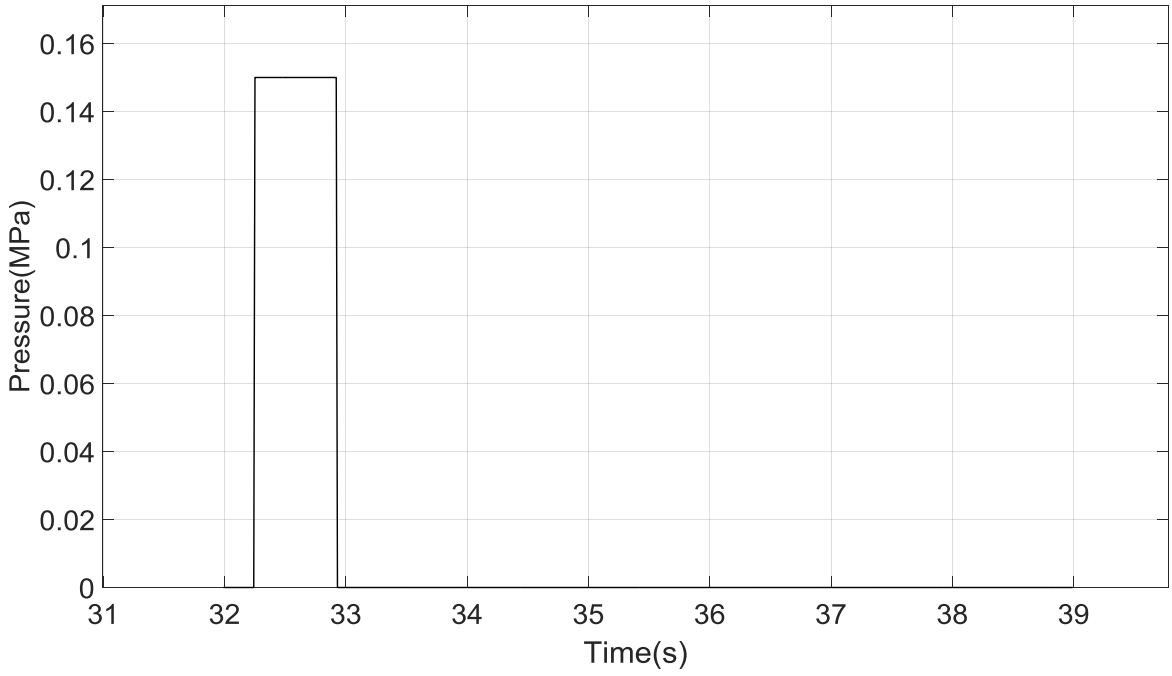

Fig. 53. Second actuator's rear side pressure.

As illustrated in Fig. 52, X position of the end-effector passed the limit during the $32 - 33(s)$. Therefore, as illustrated in Fig. 53, rear side of the second actuator is pressurized to notify and prevent passing the end-effector's boundaries.

4.1. Summary

Chapter 4 presented the results of the experimental studies. First, a T-shape link is used in order to get some experiences with pneumatic actuated systems. Then, haptic device experiment components were explained. The result of position calculation from rotary sensor were presented. Then, an experiment was done with the haptic device by using a simple spring model to simulate the tissue. Finally, haptic device work space were limited with some boundaries, in which a force would be used to notify the operator that the end effector had crossed the boundaries.

5. CONCLUSIONS

5.1. Contributions Made in This Thesis

In this thesis, a pneumatically enabled haptic device was designed and prototyped. First, three arm-actuating configurations were presented and analyzed in the sense of kinematics. Seconds, multiple arm structures were combined together to form a device. The devices were then analyzed to obtain their workspace and force capabilities. Three prototypes were then made. The final prototype was designed to operate inside the MRI room and provided 6-DOFs in comparison to the previous research in the literature that provided only a few DOFs for haptic devices that operate inside the MRI room. The final prototype device has the following characteristics:

- The device was made of Acrylic, bolts, nuts, ball bearings and trust bearings that are commercially available.
- Acrylic parts were all made by laser cutting which results in rapid prototyping of the device.
- Pneumatic actuators were used to actuate the haptic device. They have low maintenance costs, high power-to-weight ratio, are commercially available in non-magnetic materials, easy to use and wash down.
- The structure has a symmetrical workspace within the actuators stroke. It is designed in a way that is able to compensate for the required forces with the minimum actuator force.
- The end effector orientation is decoupled from its position.
- The device is small enough to fit within a 1.5 ft cube, has less than 1.5 kg weight and it is able to generate the maximum force of 1.96 lbf (8.75 N) at its end-effector.

5.2. Future Work

Possible future improvements are as follows:

- Some changes can be done for the design of device to reduce the resistance of pneumatic tubes and wires.
- The further evaluations for the device can be done by doing surgical trainings and getting some feedbacks from the surgeons.
- There are more complicated and multi layers tissue models that can be run in second environment. This provide rather realistic interaction with the tissue models.
- The designed device uses the smallest possible pneumatic actuator which has 12.5 mm stroke. It can be scaled up to use bigger actuators which brings even higher force capability to the device.
- All of the parts used in device including bolts, nuts, ball bearings and actuators are available in non-magnetic material. Therefore, a non-magnetic version of the device can be made.
- There are other possible interface methods between the master and slave devices that can be ran on the device such as position, position.

APPENDIX: THE DEVICE JOINT AND LINK SPECIFICATIONS

Following figures show detailed design of the device prototype.

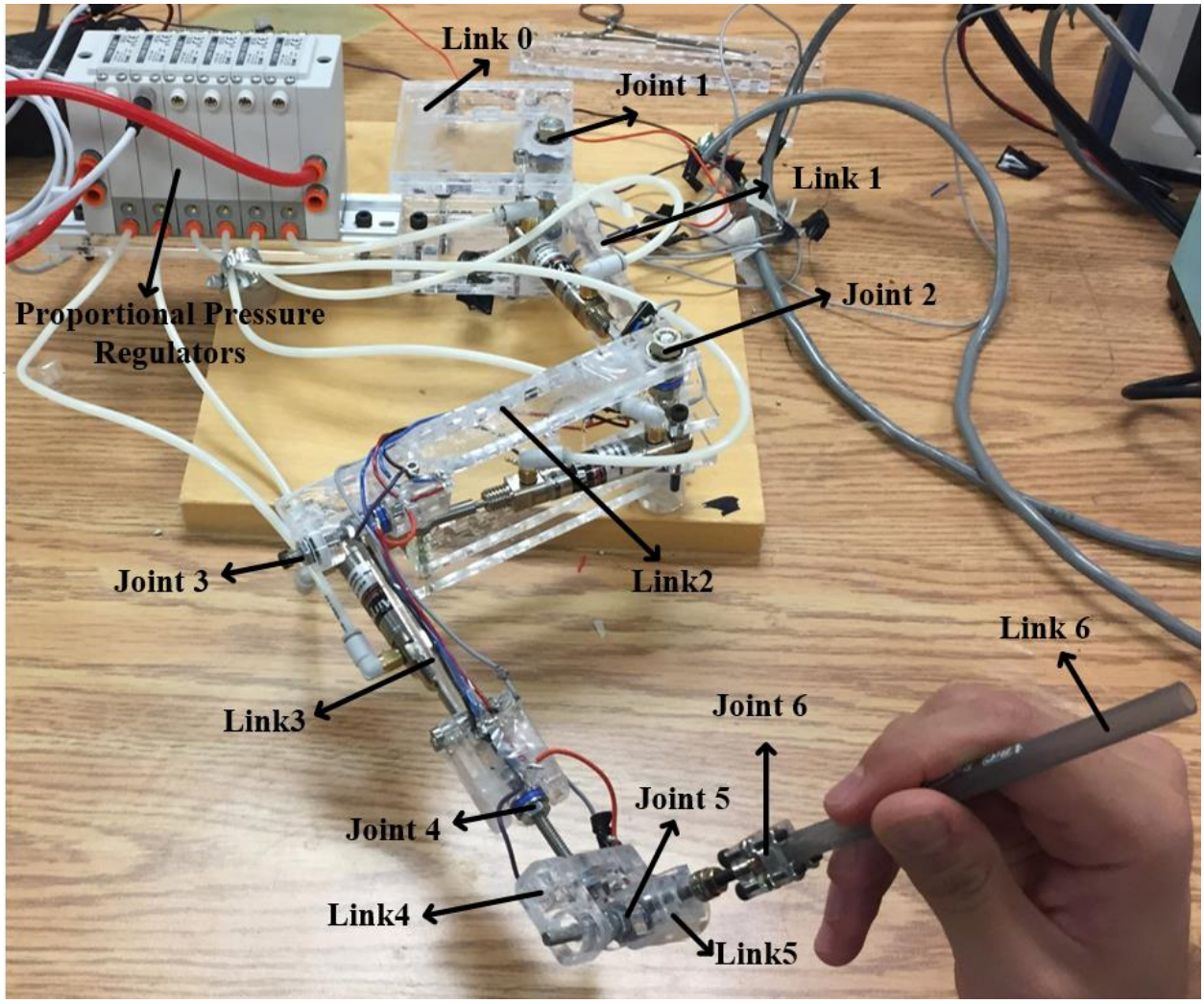

Fig. A. 1. Device joint and link specifications.

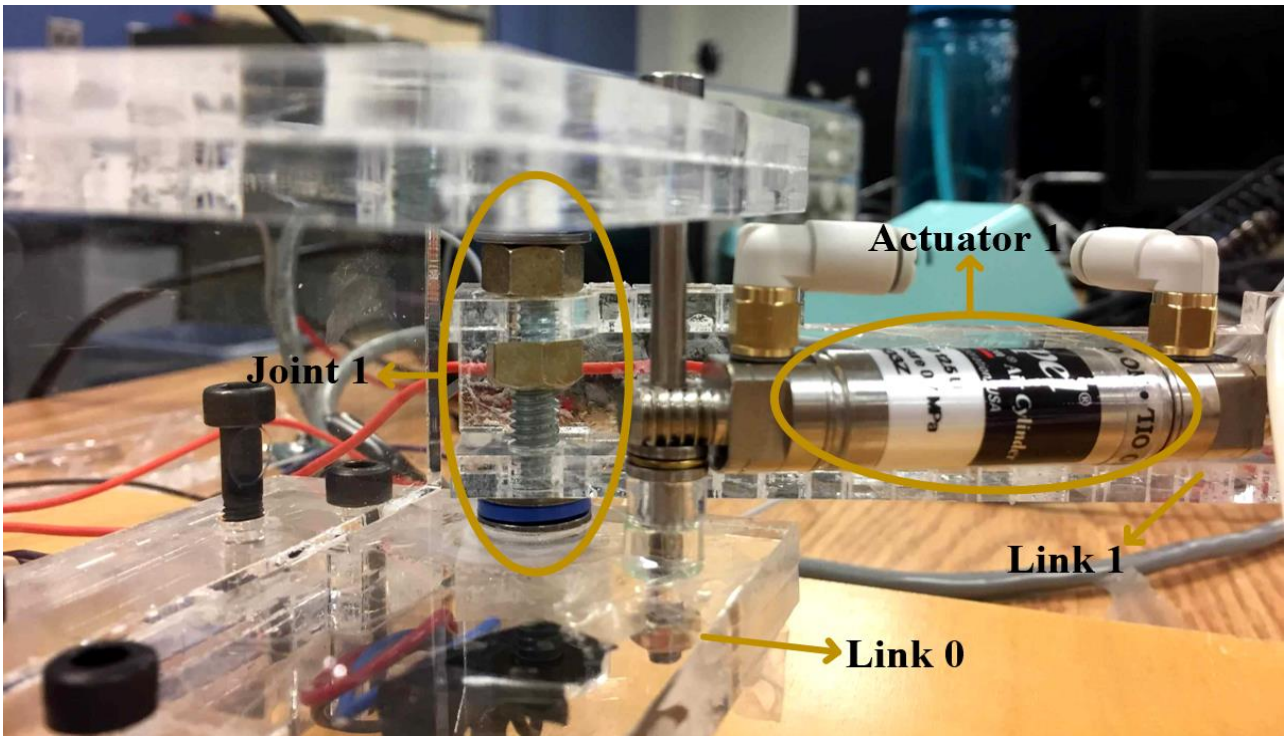

Fig. A. 2. Device prototype, first joint specification.

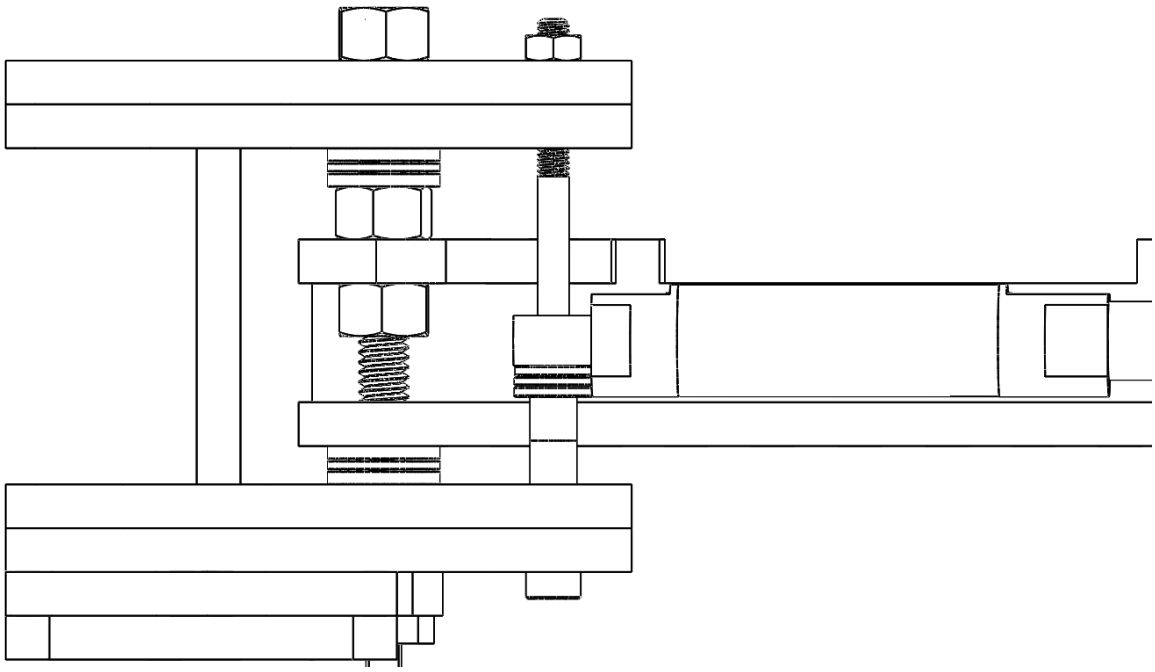

Fig. A. 3. Design of device, first joint specification.

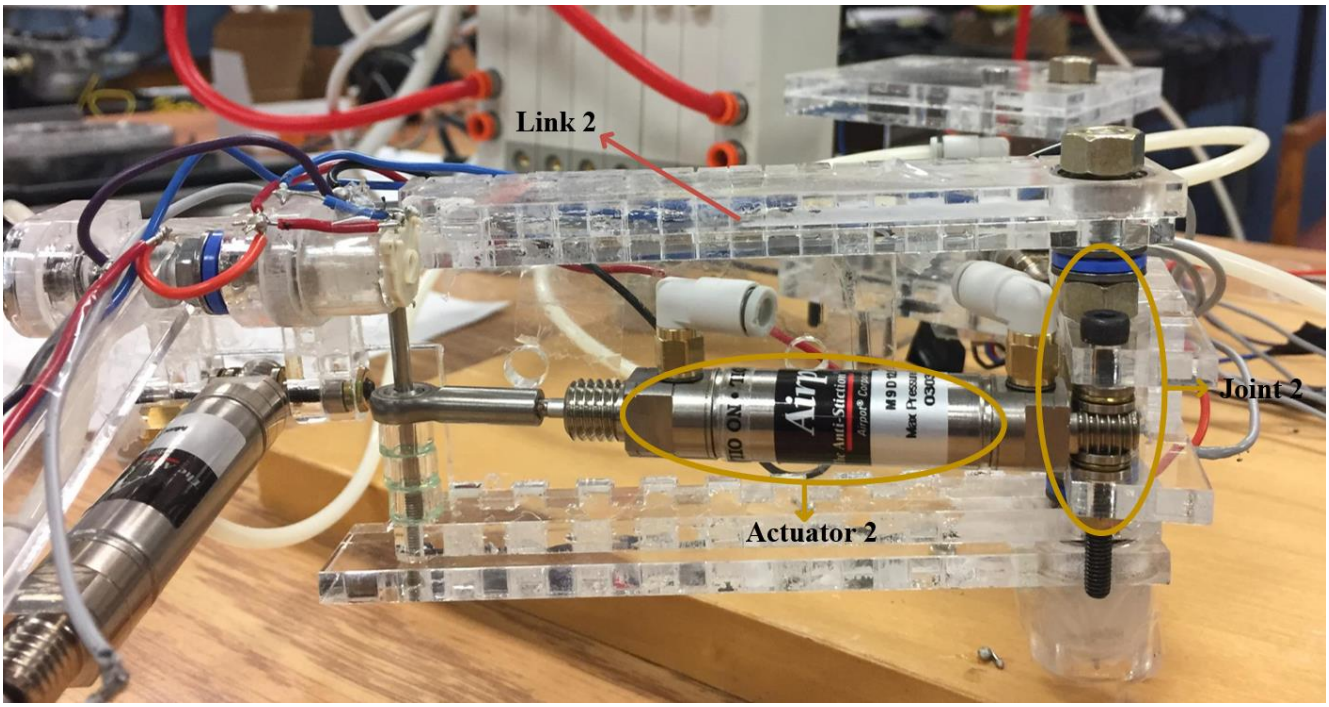

Fig. A. 4. Device prototype, second joint specification.

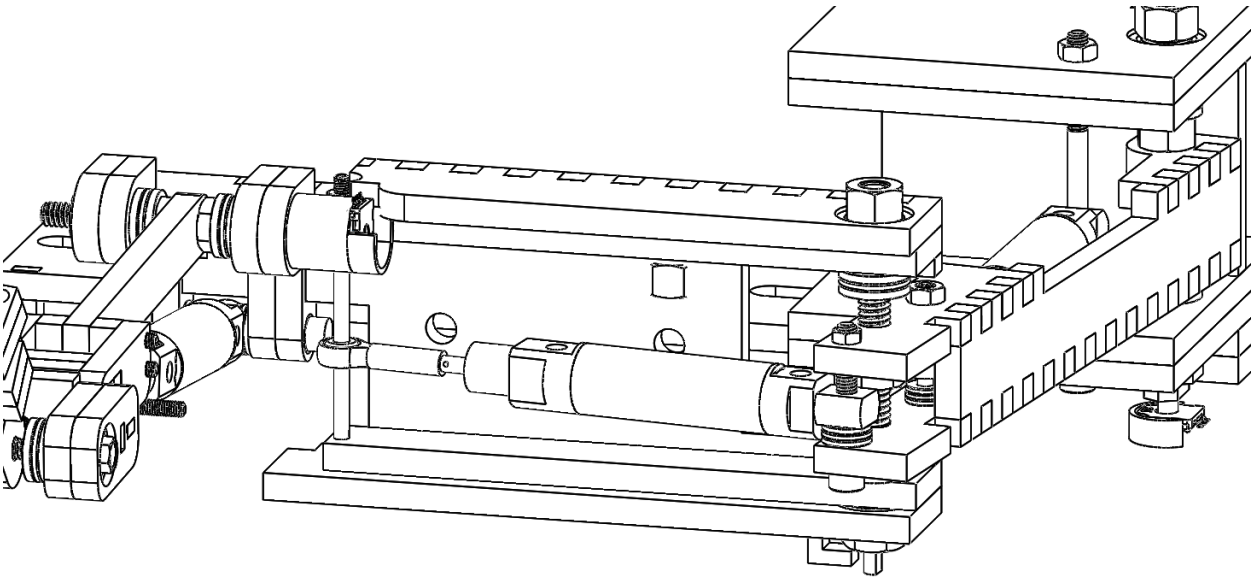

Fig. A. 5. Design of device, second joint specification.

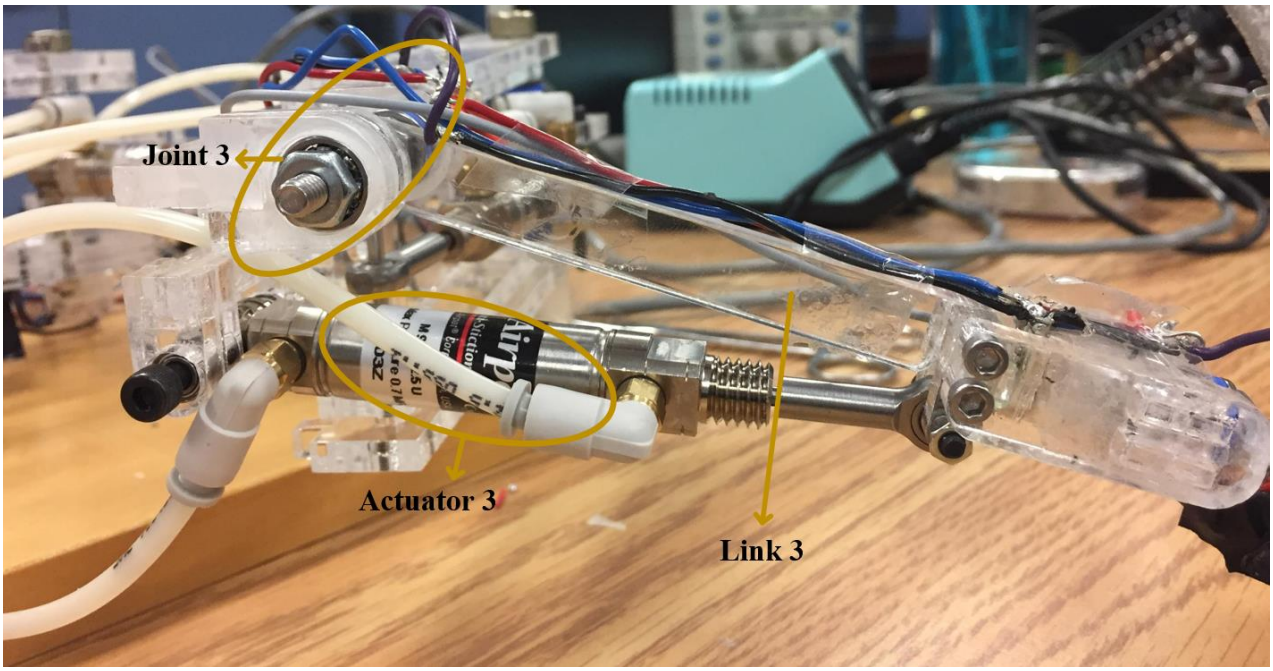

Fig. A. 6. Device prototype device, third joint specification.

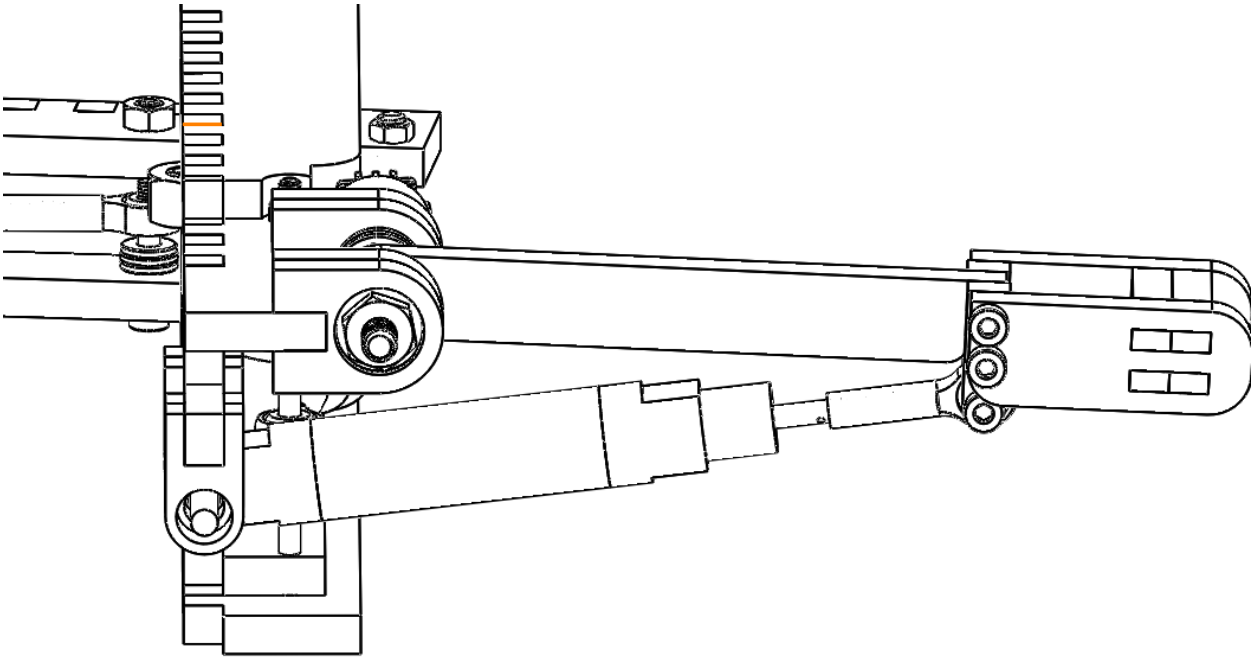

Fig. A. 7. Design of device, third joint specification.

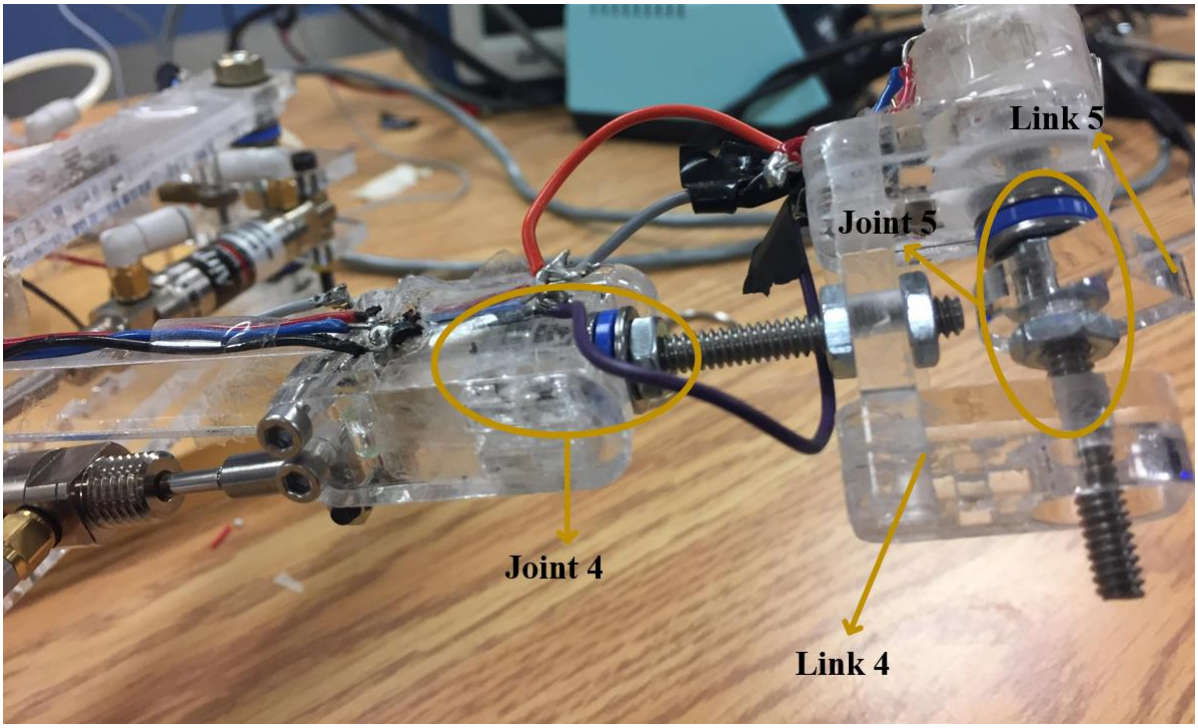

Fig. A. 8. Device prototype, fourth and fifth joint specification.

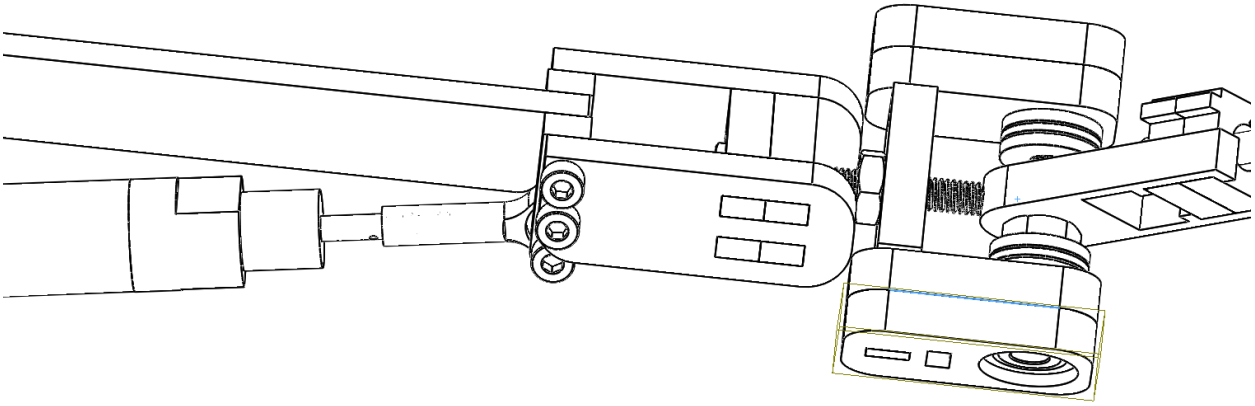

Fig. A. 9. Design of device, fourth and fifth joint specification.

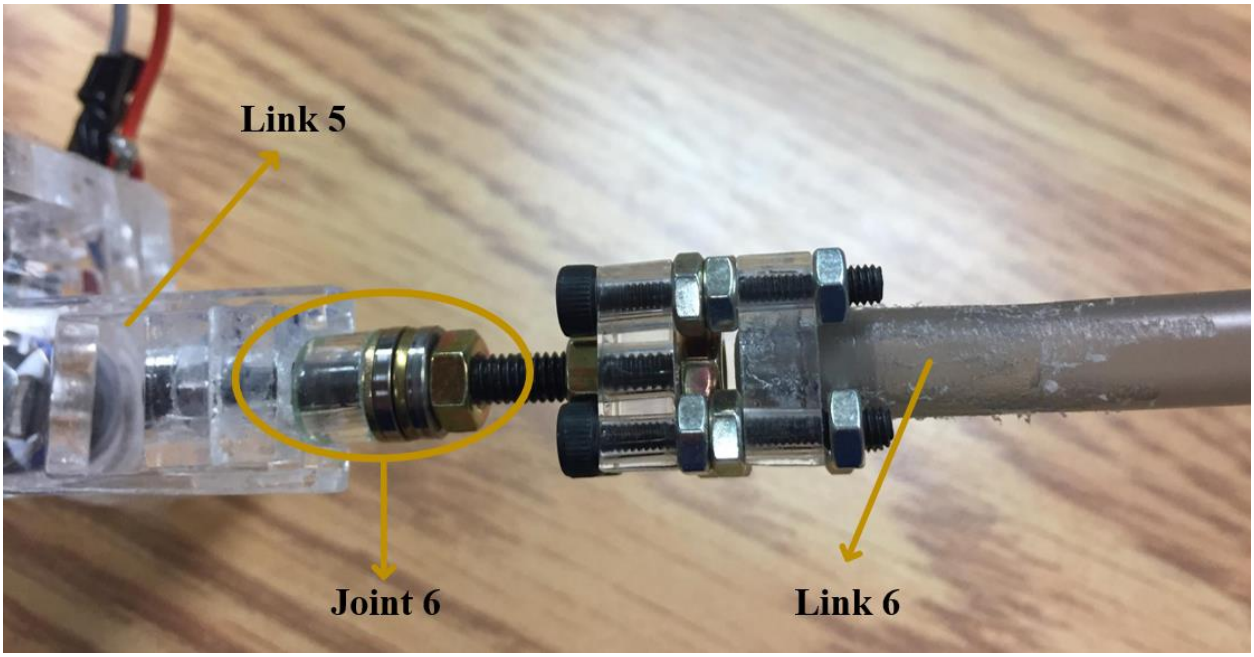

Fig. A. 10. Device prototype, sixth joint specification.

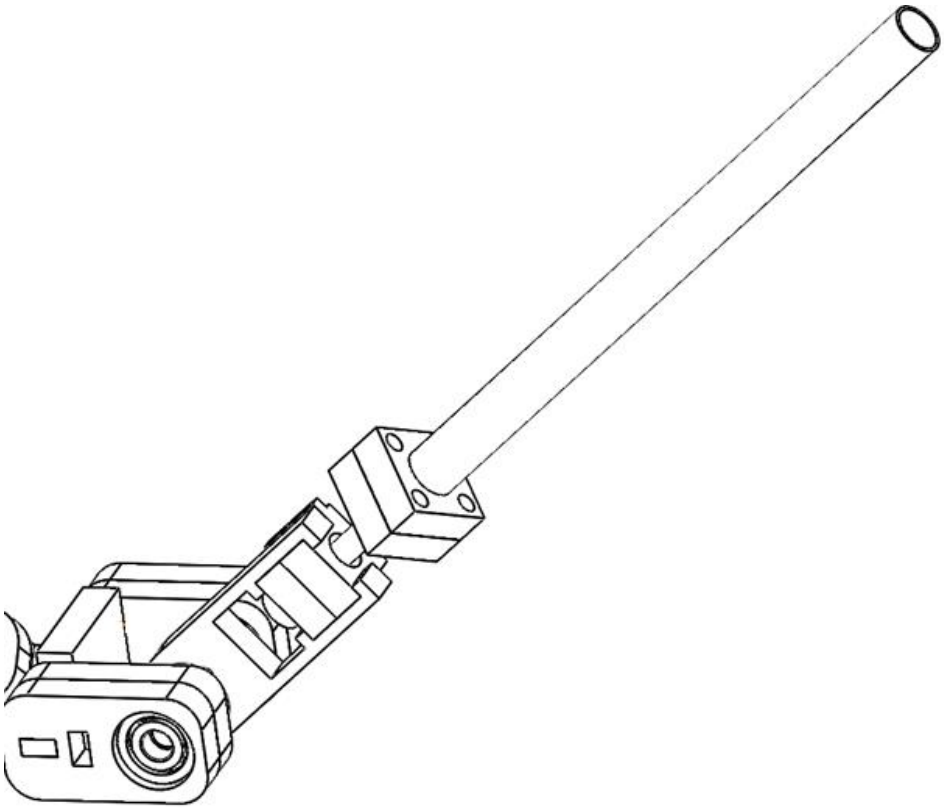

Fig. A. 11. Design of device, sixth joint specification.

6. REFERENCES

[1] R. J. Anderson and M. W. Spong, "Bilateral control of teleoperators with time delay," *IEEE Trans. Autom. Control*, vol. 34, no. 5, pp. 494–501, 1989.

[2] C. Preusche, T. Ortmaier, and G. Hirzinger, "Teleoperation concepts in minimal invasive surgery," *Control Eng. Pract.*, vol. 10, no. 11, pp. 1245–1250, 2002.

[3] B. Yang, U.-X. Tan, A. B. McMillan, R. Gullapalli, and J. P. Desai, "Design and Control of a 1-DOF MRI-Compatible Pneumatically Actuated Robot With Long Transmission Lines," *IEEEASME Trans. Mechatron.*, vol. 16, no. 6, pp. 1040–1048, Dec. 2011.

[4] N. Yu and R. Riener, "Review on MR-compatible robotic systems," in *Biomedical Robotics and Biomechatronics, 2006. BioRob 2006. The First IEEE/RAS-EMBS International Conference on*, 2006, pp. 661–665.

[5] R. Abd. Rahman, "Dynamical Adaptive Backstepping-Sliding Mode Control for servo-pneumatic positioning applications: controller design and experimental evaluation," Feb. 2016.

[6] F. Najafi and N. Sepehri, "A novel hand-controller for remote ultrasound imaging," *Mechatronics*, vol. 18, no. 10, pp. 578–590, Dec. 2008.

[7] F. Najafi and N. Sepehri, "A robotic wrist for remote ultrasound imaging," *Mech. Mach. Theory*, vol. 46, no. 8, pp. 1153–1170, Aug. 2011.

[8] A. Barrow and W. Harwin, "Design and Analysis of a Haptic Device Design for Large and Fast Movements," *Machines*, vol. 4, no. 1, p. 8, Mar. 2016.

[9] S. Salcudean, "Control for teleoperation and haptic interfaces," *Control Probl. Robot. Autom.*, pp. 51–66, 1998.

[10] F. Najafi and N. Sepehri, "Design and Prototyping of a Force-Reflecting Hand-Controller for Ultrasound Imaging," *J. Mech. Robot.*, vol. 3, no. 2, p. 021002, 2011.

[11] G. Hirzinger, B. Brunner, J. Dietrich, and J. Heindl, "Sensor-based space robotics-ROTEX and its telerobotic features," *IEEE Trans. Robot. Autom.*, vol. 9, no. 5, pp. 649–663, 1993.

[12] N. R. Parker, S. E. Salcudean, and P. D. Lawrence, "Application of force feedback to heavy duty hydraulic machines," in *Robotics and Automation, 1993. Proceedings., 1993 IEEE International Conference on*, 1993, pp. 375–381.

[13] T. Hirabayashi, J. Akizono, T. Yamamoto, H. Sakai, and H. Yano, "Teleoperation of construction machines with haptic information for underwater applications," *Autom. Constr.*, vol. 15, no. 5, pp. 563–570, Sep. 2006.

[14] M. Cenk Çavuşoğlu, W. Williams, F. Tendick, and S. Shankar Sastry, "Robotics for telesurgery: second generation Berkeley/UCSF laparoscopic telesurgical workstation and looking towards the future applications," *Ind. Robot Int. J.*, vol. 30, no. 1, pp. 22–29, Feb. 2003.

[15] S. Yadav and R. V. Krishnaiah, "Haptic science and technology," *ArXiv Prepr. ArXiv13090185*, 2013.

[16] K. Salisbury and C. Tarr, "Haptic rendering of surfaces defined by implicit functions," in *ASME Dynamic Systems and Control Division*, 1997, vol. 61, pp. 61–67.

[17] H. S. Kim, "Kinematically Redundant Parallel Haptic Device with Large Workspace," *Int. J. Adv. Robot. Syst.*, vol. 9, no. 6, p. 260, Dec. 2012.

[18] B. Siciliano and O. Khatib, *Springer handbook of robotics*. Springer, 2016.

[19] School of Electrical Engineering and Electronic Information, Xihua University, No.999, Jinzhou Road, Jinniu District, Chengdu 610039, P.R. China, R. Kong, X. Dong, and X. Liu,

"Position and Force Control of Teleoperation System Based on PHANTOM Omni Robots," *Int. J. Mech. Eng. Robot. Res.*, 2016.
[20] "Kinematics modeling of Geomagic Touch X haptic device based on adaptive parameter identification - IEEE Xplore Document." [Online]. Available: http://ieeexplore.ieee.org/abstract/document/7784042/?part=1. [Accessed: 21-May-2017].
[21] "Geomagic Phantom Premium Overview." [Online]. Available: http://www.geomagic.com/en/products/phantom-premium/overview. [Accessed: 21-May-2017].
[22] L. E. Pfeffer, O. Khatib, and J. Hake, "Joint torque sensory feedback in the control of a PUMA manipulator," *IEEE Trans. Robot. Autom.*, vol. 5, no. 4, pp. 418–425, 1989.
[23] W. Khalil and E. Dombre, *Modeling, Identification and Control of Robots*. Burlington: Elsevier, 2004.
[24] "Force Dimension - products." [Online]. Available: http://www.forcedimension.com/products. [Accessed: 17-Aug-2017].
[25] M. H. Vu and U. J. Na, "A New 6-DOF Haptic Device for Teleoperation of 6-DOF Serial Robots," *IEEE Trans. Instrum. Meas.*, vol. 60, no. 11, pp. 3510–3523, Nov. 2011.
[26] K. Suleman, K. Andersson, and J. Wikander, "A design approach for a new 6-dof haptic device based on parallel kinematics," in *Mechatronics, 2009. ICM 2009. IEEE International Conference on*, 2009, pp. 1–6.
[27] P. Boscariol, A. Gasparetto, R. Vidoni, and V. Zanotto, "A delayed force-reflecting haptic controller for master–slave neurosurgical robots," *Adv. Robot.*, vol. 29, no. 2, pp. 127–138, Jan. 2015.
[28] F. Suárez-Ruiz, I. Galiana, Y. Tenzer, L. P. Jentoft, R. D. Howe, and M. Ferre, "Grasp mapping between a 3-finger haptic device and a robotic hand," in *International Conference on Human Haptic Sensing and Touch Enabled Computer Applications*, 2014, pp. 275–283.
[29] F. Conti, J. Park, and O. Khatib, "Interface design and control strategies for a robot assisted ultrasonic examination system," in *Experimental Robotics*, 2014, pp. 97–113.
[30] S. Soyguder and T. Abut, "Haptic industrial robot control with variable time delayed bilateral teleoperation," *Ind. Robot Int. J.*, vol. 43, no. 4, pp. 390–402, Jun. 2016.
[31] R. Aras, Y. Shen, and A. Noor, "Quantitative assessment of the effectiveness of using display techniques with a haptic device for manipulating 3D objects in virtual environments," *Adv. Eng. Softw.*, vol. 76, pp. 43–47, Oct. 2014.
[32] A. Rossi, A. Trevisani, and V. Zannotto, "A telerobotic haptic system for minimally invasive stereotactic neurosurgery," *Int. J. Med. Robot.*, vol. 01, no. 02, p. 64, 2005.
[33] Y. Cheung and J. H. Chung, "Adaptive force reflecting teleoperation with local intelligence," *Ind. Robot Int. J.*, vol. 34, no. 3, pp. 201–210, May 2007.
[34] H. Mayer, I. Nagy, A. Knoll, E. U. Braun, R. Bauernschmitt, and R. Lange, "Haptic feedback in a telepresence system for endoscopic heart surgery," *Presence Teleoperators Virtual Environ.*, vol. 16, no. 5, pp. 459–470, 2007.
[35] "A Force Reflective Master-Slave System for Minimally Invasive Surgery - IROS03.pdf." [Online]. Available: http://s3.amazonaws.com/academia.edu.documents/43971371/IROS03.pdf?AWSAccessKeyId=AKIAIWOWYYGZ2Y53UL3A&Expires=1495835145&Signature=05jt6Q%2FpjIeAgDAhinGa%2FnMkMP4%3D&response-content-disposition=inline%3B%20filename%3DA_force_reflective_master-slave_system_f.pdf. [Accessed: 26-May-2017].

[36] Y.-Y. Liao, L.-R. Chou, T.-J. Horng, Y.-Y. Luo, K.-Y. Young, and S.-F. Su, “Force reflection and manipulation for a VR-based telerobotic system,” *Proc.-Natl. Sci. Counc. Repub. CHINA PART Phys. Sci. Eng.*, vol. 24, no. 5, pp. 382–389, 2000.
[37] L. J. Stocco, S. E. Salcudean, and F. Sassani, “Optimal kinematic design of a haptic pen,” *IEEEASME Trans. Mechatron.*, vol. 6, no. 3, pp. 210–220, 2001.
[38] M.-Q. Le, M. T. Pham, M. Tavakoli, and R. Moreau, “Sliding mode control of a pneumatic haptic teleoperation system with on/off solenoid valves,” in *Robotics and Automation (ICRA), 2011 IEEE International Conference on*, 2011, pp. 874–879.
[39] “Customizable Pneumatic Actuators, Dashpot & Snubber Experts - Airpot Corporation.” [Online]. Available: http://airpot.com/. [Accessed: 07-Jun-2017].
[40] T. Yoshikawa, “Manipulability of robotic mechanisms,” *Int. J. Robot. Res.*, vol. 4, no. 2, pp. 3–9, 1985.
[41] “Airpel Double-Acting Universal Mount,” *Customizable Pneumatic Actuators, Dashpot & Snubber Experts - Airpot Corporation*. [Online]. Available: http://airpot.com/product/airpel-double-acting-universal-mount-4/. [Accessed: 06-Jul-2017].
[42] “14-15-E-ITV.indd - ITV.pdf.” [Online]. Available: http://www.smcpneumatics.com/pdfs/ITV.pdf. [Accessed: 06-Jul-2017].
[43] “PLC Center MRO Inventory and Industrial Repair Service - Radwell.ca.” [Online]. Available: http://www.radwell.ca/en-CA/. [Accessed: 06-Jul-2017].
[44] “Bourns - Bourns - Home.” [Online]. Available: http://www.bourns.com/. [Accessed: 07-Jul-2017].